

Tidally Driven Oscillations in  
KIC 4544587: a  $\delta$  Scuti Binary System

by

Kelly Marie Hambleton

September 2011

A thesis submitted in partial fulfilment of the requirements for the degree of Master of Science  
(by Research) in Astrophysics at the University of Central Lancashire.

## Student Declaration

### Concurrent registration for two or more academic awards

I declare that while registered for the research degree, I was with the University's specific permission, an enrolled student for the following award:

\_\_\_\_\_ Certificate in Languages in Beginners Spanish \_\_\_\_\_

### Material submitted for another award

I declare that no material contained in the thesis has been used in any other submission for an academic award and is solely my own work

Signature of Candidate \_\_\_\_\_

Type of Award \_\_\_\_\_ MSc (by Research) in Astrophysic \_\_\_\_\_

School \_\_\_\_\_ CEPS \_\_\_\_\_

## Abstract

Binary modelling techniques and frequency analysis have been applied to the *Kepler* photometric observations of KIC 4544587 to determine information about the orbital characteristics, individual components and tidal interactions. The system contains an early A-type  $\delta$  Scuti variable, which pulsates in both pressure and gravity modes, and a late F- to early G-type star, which is possibly a solar-like oscillator. The Wilson-Devinney code was used to model the Quarter 3.2 data and PHOEBE was used to model the Quarter 7 data; the results of these two methods were then compared. Using PHOEBE the rate of apsidal advance was determined to be  $0.0001179(1)\text{rad d}^{-1}$ , which gives  $145.9(1)\text{yr}$  for a complete precession.

Subsequently the binary model light curve was subtracted from the original data and frequency analysis was performed on the residuals. Fifteen frequencies were identified that are harmonics of the orbital period, 9 of which are in the g mode regime and 6 in the p mode regime. It was concluded that these frequencies are not an artifact of the model fit and thus are a signature of tidal resonance. It was also determined that many of the frequencies in the p mode regime are separated from the two dominant p modes by a multiple of the orbital frequency; six of the identified modes demonstrate this separation to an accuracy of  $3\sigma$ . As they are not orbital harmonics, the origin of these frequencies remains unknown. Currently we know of no other star demonstrating these characteristics.

# Contents

<b>1</b>	<b>Introduction</b>	<b>1</b>
1.1	Binary Systems . . . . .	1
1.2	Delta Scuti Stars . . . . .	3
1.3	Binary Systems with $\delta$ Scuti Components . . . . .	6
1.4	Tidal Interactions . . . . .	6
1.5	Asteroseismology . . . . .	8
1.6	Tidally Induced Pulsations . . . . .	10
1.7	Kepler Mission . . . . .	11
<b>2</b>	<b>Observations of KIC 4544587</b>	<b>13</b>
<b>3</b>	<b>Identification of the Orbital Period</b>	<b>16</b>
3.1	Phase Dispersion Minimisation . . . . .	16
<b>4</b>	<b>Binary Modelling</b>	<b>19</b>
4.1	Binary model parameters . . . . .	20
4.2	JKTEBOP . . . . .	26
4.2.1	Implementation of JKTEBOP to KIC 4544587 . . . . .	26
4.3	Wilson and Devinney . . . . .	27
4.3.1	Binning the data . . . . .	28
4.3.2	Constraining the Model using WD . . . . .	28
4.4	Multiple Iterations . . . . .	29
4.4.1	Generation of Residuals . . . . .	31
4.5	PHOEBE . . . . .	33
4.5.1	Constraining the Model and Generation of Residuals using PHOEBE . . . . .	34
4.5.2	The Synchronicity Parameter . . . . .	35
4.5.3	Apsidal Motion . . . . .	38
4.6	Comparison of Quarter 3.2 and Quarter 7 Results . . . . .	40
<b>5</b>	<b>Frequency analysis</b>	<b>43</b>
5.1	Identification of Pulsation Frequencies . . . . .	43
5.1.1	Period-Density Relation . . . . .	46
5.2	Indications of Tidal Interactions . . . . .	47
5.2.1	Frequency Separation Within the p Mode Regime . . . . .	49

5.3 Wavelet analysis . . . . .	51
<b>6 Conclusions</b>	<b>55</b>
<b>7 Acknowledgements</b>	<b>57</b>
<b>A Appendix</b>	<b>62</b>

# 1 Introduction

In stellar astrophysics binary systems are considered fundamental to our understanding of the stellar structure and evolution of single stars. As more than 50% of all stars are known to be in multiple systems (Pigulski, 2006), an important aspect of binary star analysis is the understanding of binary stars themselves. Through the analysis of binary systems we can not only unveil information about the masses and structure of the individual components and determine distances, but we can also investigate phenomena that occur due to the binarity of a system. These include: mass transfer between the stellar components, which can lead to novae and recurrent novae and consequently enable the investigation of binary systems as the progenitors of type Ia supernovae; the study of x-ray binaries; the formation of common envelopes; and even the eventual merging of stellar components to form an individual star.

Another interesting physical phenomenon that occurs in binary systems is the exchange between the system's orbital and rotational angular momentum. This generates an increase in the orbital angular momentum of the system, which causes the stellar orbit to increase in size whilst decreasing the rotational velocity of the stellar components. Eventually, the binary system enters a minimum energy configuration where the stars are in a circular orbit and the duration of a single orbit is equal to that of a complete stellar rotation: the orbit is synchronous. Consequently, it has been observed, by Abt & Hudson (1971), that A stars in short period binaries have slower rotation than their single counterparts.

The energy dissipation mechanism that causes this reduction in rotational angular momentum, as the stars tend towards pseudo-synchronous and eventually synchronous rotation, has been attributed to two processes. For low mass stars with convective outer envelopes it is theorised that the coupling of the tidal flows and the turbulent eddies in the convective stellar surface layer cause the dissipation of energy within the system (Zahn, 1977). For high mass stars with radiative outer envelopes Zahn (1975) hypothesised that oscillations are generated in the outer envelope due to the variation in gravitational field causing energy to dissipate. This is known as radiative damping.

The theory of radiative damping suggests that through the generation of dynamic tides on the stellar surface the energy of a system and thus stellar rotation rates are reduced. These dynamic tides are theorised to be periodic oscillations with buoyancy acting as the restoring force, as hypothesised by Cowling (1941) for the non-dissipative case. The oscillation modes are determined by natural eigenfrequencies inherent to the star, specifically the star's intrinsic properties as a gravity (g) mode oscillator (where the restoring force is buoyancy). Subsequently, if a resonance occurs between a natural eigenfrequency of a star and a tidal forcing frequency of the binary system, the oscillation amplitudes can be significantly amplified.

Almost 40 years after Zahn (1975) proposed the theory of radiative damping, only a small number of cases exist that demonstrate resonant excitation. Thus there is only a limited amount of direct evidence for the existence of dynamic tides as an energy dissipation mechanism. The motivation of this work is the investigation and potential confirmation of resonantly excited pulsations in the revolutionary *Kepler* photometric observations of KIC 4544587.

## 1.1 Binary Systems

The Vogt-Russell Theorem states that the structure and evolution of a star may be determined through knowledge of the initial mass and chemical composition alone (Vogt, 1926). It is through the analysis

of binary star systems that this and other information about stellar bodies can be precisely acquired. Consequently, binary systems form the fundamental building blocks upon which we base our current understanding of stellar astrophysics.

The mass of a star can range from  $\sim 0.08 M_{\odot}$ , the lowest mass where hydrogen fusion can occur, to  $\sim 120 M_{\odot}$ , the Eddington limit (Eddington, 1930), which is the limiting mass where a stellar component is theoretically able to remain in radiative equilibrium. On the other hand, from observations of the R136 cluster it has been inferred from the effective temperatures of the stellar components that many stars have masses greater than  $150 M_{\odot}$  (Crowther et al., 2010). It is only through the dynamics of binary systems that precise masses can be directly measured, without any assumptions other than Newtonian dynamics. Moreover, with a spectroscopically detectable companion, the masses of the stellar components can be determined to an accuracy of  $\sim 3\%$ . The most recent catalogue of stellar masses that have been accurately determined from binary systems was generated by Torres et al. (2010) where the masses have been obtained for 190 stars to an accuracy of 3% or better. Such an accurate understanding of stellar masses is imperative for the advancement of stellar models. Furthermore, it enables the rejection of models by virtue of incorrect physical assumptions alone, a feature that is not typical in astronomy.

Fig. 1 depicts a radial velocity curve from which the masses of the stellar components can be determined. The criteria for the Torres et al. (2010) catalogue are that the observed radial velocity curves must have more than 25 points with a real uncertainty of less than  $1 \text{ km s}^{-1}$ . Consequently, this well defined radial velocity curve requires more data points before reaching the standard required by Torres et al. (2010) which have been adopted after those specified by Andersen (1991). It is also worth noting that the masses of binary components can be determined using alternative methods that do not require radial velocities. However, such assessments require the combination of the angular orbital separation with parallax or spectroscopic information, which adds significantly to the uncertainty involved (Andersen, 1991).

If the line of sight is aligned with the orbital plane, such that the star is eclipsing, we are also able to determine the radii of the stellar components to an accuracy of  $\sim 3\%$ . This is done by analysing the light curve using binary modelling techniques. To determine the radii to such remarkable accuracies, knowledge of the eccentricity, argument of periastron, temperature and luminosity ratios must be accurately acquired through photometry and spectroscopy. Furthermore, the rate of apsidal advance may also be required if it is large enough to have an impact on the determination of the radii.

From the values obtained, a tight correlation between mass and luminosity has been determined (Andersen, 1991). Equally, there is a strong correlation between mass, radius and  $\log g$ , from which  $\log g$  values can be obtained to an accuracy greater than that currently obtained through spectroscopy. Temperatures are not accurately determined using these parameters as the main-sequence mass for a star can vary by up to 40% for a given temperature (Torres et al., 2010).

Empirical formulae have been generated, by Torres et al. (2010), as a consequence of these correlations, which allow for the determination of the mass and radius of a single star through the knowledge of its effective temperature, luminosity and metallicity (values that can be obtained through spectroscopy):

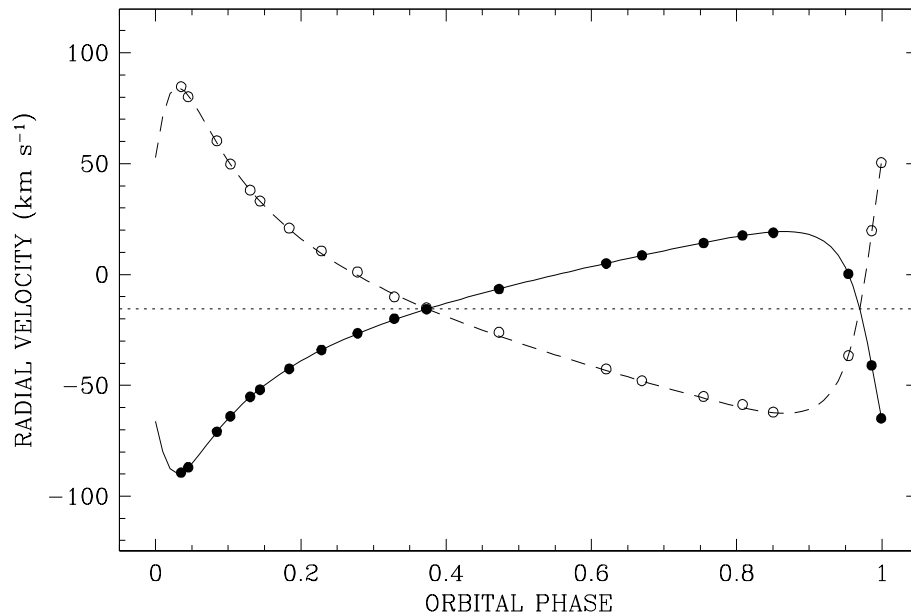


Figure 1: A double lined radial velocity curve of KIC 3749404, a binary with a spectroscopically detectable companion. The black dots represent the more massive, primary component, and the circles represent the secondary. Despite the fact that this radial velocity curve is well defined, it does not contain enough data points, as specified by Torres et al. (2010), to determine the mass to an accuracy of 3%.

$$\log M = 1.56(6) + 1.38(3)X + 0.42(3)X^2 + 1.1(2)X^3 - 0.14(1)(\log g)^2 + 0.019(2)(\log g)^3 + 0.10(1)[\text{Fe}/\text{H}] \quad (1)$$

$$\log R = 2.44(4) + 0.66(2)X + 0.17(3)X^2 + 0.7(1)X^3 - 0.214(7)(\log g)^2 + 0.023(1)(\log g)^3 + 0.041(8)[\text{Fe}/\text{H}] \quad (2)$$

where  $X = \log T_{\text{eff}} - 4.1$  and the values in the parentheses are the uncertainties in the final digit. The uncertainties associated with these values, estimated from the scatter in the correlations, are 6.4% and 3.2% for the masses and radii respectively.

The knowledge of empirical values to such a high accuracy enables us to probe the interactions between stars and their environments, and further understand internal processes such as nucleosynthesis. Moreover, as the components of a binary system form simultaneously and from the same material, they are identical in both metallicity and age, and thus they provide an ideal laboratory for probing stellar evolution, enabling the development of stellar evolution theory pertaining to the effect of metallicity on evolutionary phase.

## 1.2 Delta Scuti Stars

The classical instability strip is an area on the Hertzsprung-Russell Diagram within which the majority of stars pulsate. Pulsation is primarily via the  $\kappa$  mechanism, which occurs when heat is trapped inside the star due to the presence of an ionisation layer. The opacity of the ionization zone causes the

star to swell. The heat is released when the zone becomes ionised, which causes the star to return to equilibrium and the zone to return to its original state of ionisation; the process is then repeated. The instability strip is bounded by a red and blue edge, beyond which the stars cease to pulsate via this mechanism; beyond the blue edge the stars still pulsate via the  $\kappa$  mechanism, but as a consequence of their Fe ionisation zone. Pamyatnykh (1999) determined that the blue edge of the instability strip was constrained by the helium opacity bump, and later Houdek (2000) discovered that the red edge was determined by convection.

Delta Scuti stars form an integral part of the instability strip, spanning all stages of evolution from pre-main sequence to approximately 2 magnitudes above the main sequence (Rodríguez & Breger, 2001), which can be seen in Fig. 2. Their luminosities range from  $0.6 < \log(L/L_{\odot}) < 2.0$  corresponding to an effective temperature range of  $3.8 < \log(T/T_{\odot}) < 3.95$  (Buzasi et al., 2005). They oscillate in radial and non-radial modes in both p and low order g modes with observed periods ranging from 0.012 d to 0.35 d (Amado et al., 2004; Pamyatnykh, 2000).

Delta Scuti stars have a mass range between 1.5 and 2.5  $M_{\odot}$  (Lefèvre et al., 2009). At approximately 2  $M_{\odot}$  there is a transitional phase; stars that are more massive have radiative outer envelopes whereas stars that are less massive have convective outer envelopes. Furthermore, stars of approximately 1.5  $M_{\odot}$  develop a convective core (Aerts et al., 2010). Thus these critical phases occur within the range of masses encompassed by  $\delta$  Scuti stars. Consequently, the asteroseismic investigation of  $\delta$  Scuti stars could eventually unveil fundamental information pertaining to the physical processes that govern these transitions. For example, the depth of the convective envelope of a star can be determined through the frequency of the modes present (as a consequence of the variation in sound speed) this in turn can be related to the mass and age of the star. Furthermore, the existence of p mode oscillations and g mode oscillations and their relative time scales is related to the orientation of the convective and radiative zones present in a star.

Due to limited observing capabilities, the first  $\delta$  Scuti stars observed had relatively high amplitudes (on the order of 0.1 mag (Fath, 1940)), with modes that appeared unstable. However, following a review of many  $\delta$  Scuti stars, Kurtz (1980) argued that the apparent variability was due to the superposition of many modes, which was later found to be correct. Delta Scuti stars were then divided into categories according to their variability. These included high amplitude  $\delta$  Scuti (HADS) stars, which make up  $\sim 0.3\%$  of all  $\delta$  Scuti stars (where the criterion is  $\Delta m_v > 0.3$ ) (Lee et al., 2008) and low amplitude  $\delta$  Scuti (LADS) stars.

Initially HADS stars were defined as  $\delta$  Scuti stars that pulsated in the fundamental radial mode only and LADS stars as those that pulsate in both radial and non-radial modes. HADS stars are now known to have dominant pulsations in two radial modes: a combination of two from the fundamental mode, first and second harmonic (Aerts et al., 2010). With respect to other  $\delta$  Scuti stars, HADS demonstrate generally slow rotation rates ( $v \sin i \leq 30 \text{ kms}^{-1}$ ). Thus it is believed that HADS are primarily immediate post main sequence stars (Petersen & Christensen-Dalsgaard, 1996). Consequently the slow rotation rate is attributed to the decrease in angular momentum which is caused by the post main sequence increase in envelope size. Mathias et al. (1997) later showed that HADS stars also pulsate in non-radial modes; however, with respect to the dominant radial modes, these pulsations were observed to have very weak amplitudes.

Prior to the revision of their classification criteria by Grigahcène et al. (2010a),  $\delta$  Scuti stars were

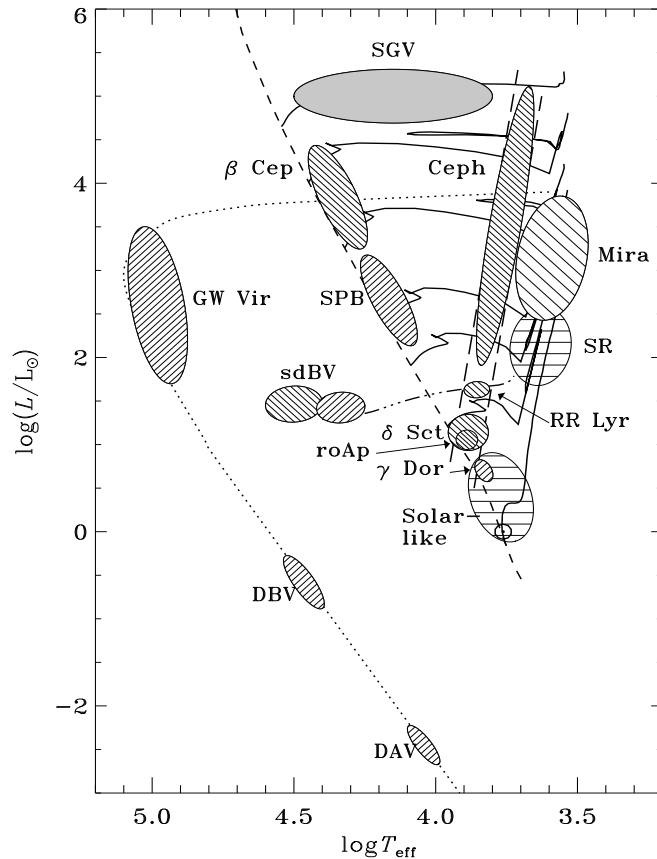


Figure 2: A pulsational H-R diagram. The  $\delta$  Scuti stars can be found on the intersection between the main sequence and the instability strip. From Aerts et al. (2010).

believed to form approximately 50 per cent of all the main sequence stars in the classical instability strip (Breger, 2000). However, with the implementation of advanced instruments such as *Kepler* (Gilliland et al., 2010), *MOST* (Walker et al., 2003) and *CoRoT* (Baglin et al., 2006), many hybrid  $\delta$  Scuti and  $\gamma$  Dor stars have been observed; thus new classification criteria, containing  $\gamma$  Dor– $\delta$  Scuti and  $\delta$  Scuti– $\gamma$  Dor hybrid stars have been introduced (Grigahcène et al., 2010a). Gamma Dor stars are defined as stars with main sequence temperatures of  $3.83 < \log(T/T_{\odot}) < 3.88$  that pulsate in high order gravity modes through convective blocking (Guzik et al., 2000); their pulsation periods are predominantly on the order of 1 d (Grigahcène et al., 2010b). Following this revision, through the characterisation of 234 stars, the percentage of  $\delta$  Scuti stars on the main sequence has now been approximated to 27% (Grigahcène et al., 2010a).

In the new classification system  $\delta$  Scuti stars are defined as stars within the aforementioned temperature range, with predominant frequencies in the frequency domain greater than  $5 \text{ d}^{-1}$ ; with lower frequencies having relatively low amplitudes (Grigahcène et al., 2010b). However, the  $\kappa$  mechanism is the primary driving mechanism of their pulsations, it is suggested by Antoci et al. (2011) that  $\delta$  Scuti stars may also pulsate with stochastically excited modes.

### 1.3 Binary Systems with $\delta$ Scuti Components

In a study of 119 A0–A9 stars  $35 \pm 5$  per cent were found to be in multiple systems (Abt, 2009). However, only 22 per cent of the  $\delta$  Scuti stars catalogued are known to be multiple stars (Rodríguez & Breger, 2001). In binary systems the rotational velocity of each stellar component tends towards a velocity that is synchronous with the orbital period. As synchronous velocity generally implies a surface velocity of less than  $120 \text{ km s}^{-1}$  (although this is dependent on the orbital period and radius of the star), the turbulence in the outer stellar envelope is significantly low; hence only a small amount of meridional mixing occurs. This allows diffusion to take place, which has been suggested to prevent pulsation through composition effects and stratification (although, equally, the lack of pulsation could enable diffusion to occur more readily) (Breger, 1970). Thus it has previously been assumed that multiplicity indirectly inhibits pulsation. On the other hand, there are several cases, including HD174884 (Maceroni et al., 2009), HD177863 (Willems & Aerts, 2002), and the more recent, extreme case of KOI–54 (Welsh et al., 2011) that demonstrate how multiplicity can not only alter, but increase pulsation amplitudes. Therefore it is also plausible that this difference is due to our inability to identify  $\delta$  Scuti stars in multiple systems.

Irrespective of the number of  $\delta$  Scuti multiple systems known, the combination of stellar parameters that can be gleaned from the multiplicity of a system, with the numerous modes of a  $\delta$  Scuti star, make these objects extremely valuable. Through the use of binary modelling techniques and pulsation analysis, an array of information is available. This includes information pertaining to the internal stellar structure and rotation, and direct measurements of stellar masses, distances and radii. Currently, the thorough asteroseismic analysis of  $\delta$  Scuti stars is rarely achieved due to the large number of oscillatory modes present in most of these objects. However, with the continuation of work in this field, it is expected that an increasing number of these intriguing objects will be solved in the foreseeable future.

### 1.4 Tidal Interactions

In a binary system, if the components are in relatively close proximity to one another, the gravitational forces between the two components can provoke tidal interactions; these are analogous to the lunar tides generated on the Earth. Moreover, if the binary is eccentric as seen in Fig. 3, the tides generated become misaligned with respect to their instantaneous equipotential shapes (Hut, 1980). This generates torque between the two components which causes an exchange of angular momentum between the orbital and stellar rotations, and further causes the system’s energy to dissipate.

Tidal interactions eventually lead to one of two outcomes: the stars spiral towards each other and eventually merge or a circularized, synchronous orbit is achieved (Hut, 1980). A synchronous orbit is defined as an orbit where the rotational and orbital velocities are equal and the equatorial planes of the stellar components are aligned with the orbital plane. It has been shown statistically by Torres et al. (2010) that the time for circularisation to occur is dependent on the radii of the stars, relative to the radius of the orbit, and also that circularisation occurs on a shorter time scale for stars with convective envelopes. Consequently, in a sample of 95 detached binaries, there were no eccentric binaries with a period less than 1.5 d (Torres et al., 2010).

One important aspect of tidal interactions, as demonstrated by Cowling (1938) and Sterne (1939), is that through the determination of the rate of apsidal advance, the constant  $k_2$  can be identified:

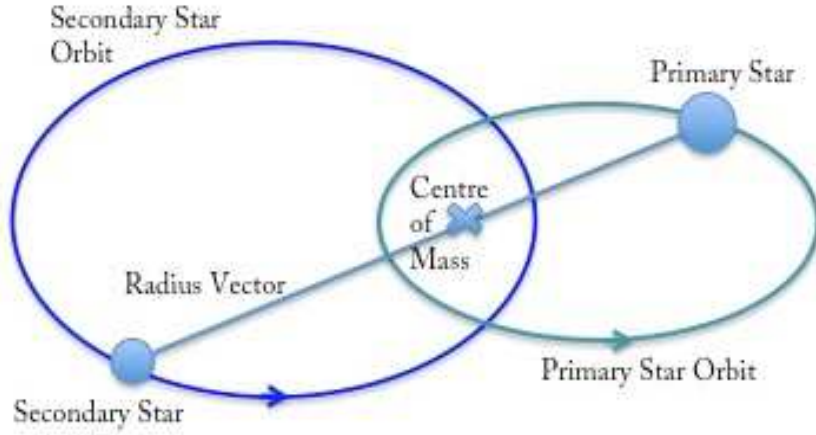


Figure 3: An eccentric binary orbit. Due to the eccentricity of the orbit, the distance between the two stars, denoted by the radius vector, varies with time. Consequently, the gravitational forces acting on the components vary as a function of phase.

$$\epsilon = \left( \frac{R_1}{r} \right)^5 \frac{m_2}{m_1} \frac{2\pi}{P_{orb}} k_2 15 f(e^2) \quad (3)$$

where  $\epsilon$  is the ratio of the period of the orbit to the rotation of the line of apsides,  $k_2$  is the numerical constant dependent on the density distribution of the stellar component,  $P_{orb}$  is the orbital period,  $r$  is the radius of the orbit and  $R_1$  is the radius of the primary and  $m_1$  and  $m_2$  are the masses of the primary and secondary components respectively,  $e$  is the eccentricity and

$$f(e^2) = (1 - e^2)^{-5} \left( 1 + \frac{3}{2}e^2 + \frac{1}{8}e^4 \right) \quad (4)$$

$k_2$  contains information about the central density of the stellar component and is also known as the dimensionless apsidal motion constant. Moreover, through the study of tidal interactions an understanding of the dynamics and energy dissipation mechanisms of binary systems, and how varying conditions determine a system's end state may be obtained.

The modelling of tidal interactions is currently computed using several different methods. One method, the equilibrium tide model (Darwin, 1880; Hut, 1980), generates the distorted stellar shapes by assuming that the gravitational-centrifugal potential of the system remains in equilibrium throughout the orbit. Overlaying this aspect of the model are considerations of the surface torque, specifically that which occurs due to the lag between the tidal bulges and the axis joining the centres of the two stars, and how this torque generates energy dissipation.

Another method is called the dynamical tide approach (Zahn, 1975; Fabian et al., 1975; Press & Teukolsky, 1977), where the stellar components are defined as oscillators. In an eccentric system, each component exerts a varying gravitational force on its companion. As these forces vary with orbital phase, the forcing frequencies generated are harmonics of the orbital frequency; some of which are likely to resonate with the star's natural eigenfrequencies. Furthermore, the stellar shape deforms significantly during periastron, which further modifies the star's normal modes. In such modelling efforts acoustic modes, gravity modes and inertial modes (where the restoring force is the Coriolis force and is usually only applicable to fast rotators) are included. Through these considerations the energy dissipation of

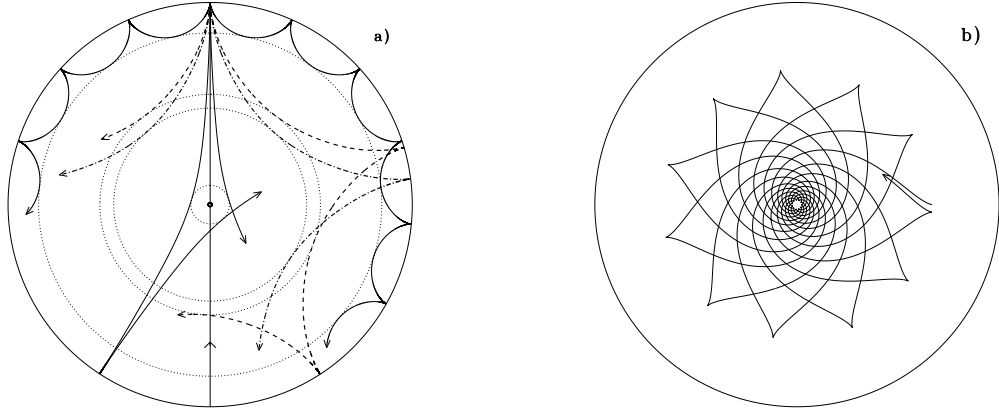


Figure 4: *Left panel (a)*: A ray diagram to demonstrate the propagation of p mode sound waves through the solar interior. The line passing through the center is indicative of a radial mode and lines of decreasing depth demonstrate the behaviour of modes with increasing  $l$  values. *Right panel (b)*: A ray diagram to demonstrate the propagation of g mode sound waves through the solar interior. Due to the convective outer layer of the sun, the g modes do not penetrate to the surface; this is not true of  $\delta$  Scuti stars where the outer envelope is radiative. From Cunha et al. (2007)

the system can be effectively analysed.

These methods rely on a priori information and assumptions. Advances are currently being made towards generating models on first principles alone. For example, Moreno et al. (2011) have generated a model where the surface layers of the stellar components are thin deformable layers, which are subject to gravitational, Coriolis and centrifugal forces, gas pressure and viscous forces. The improvement of our understanding of such interactions from direct observation is crucial to the advancement of knowledge in this area.

## 1.5 Asteroseismology

Asteroseismology is the study of stellar pulsations, analogous to seismology, the study of earthquakes. It is a technique that can be applied to intrinsically pulsating stars as a method of probing the stellar interior. There are two main types of waves generated by pulsating stars: acoustic waves, also known as p modes, where the restoring force is pressure, and gravity modes, or g modes, where the restoring force is buoyancy (Aerts et al., 2010). As these waves pass through the stellar interior, depending on the degree of the mode (a quantity related to spherical harmonics), the wave will be contained within a certain region of the star, the acoustic cavity (see Fig. 4). If the wave is not damped before it reaches the stellar surface, it will be visible to the observer as a fluctuation in both luminosity and radial velocity, presenting vital information about the region in which it is contained.

As the sound passes through the star, in an adiabatic case, the speed is determined by the pressure,  $p$ , and the density  $\rho$ :

$$c = \sqrt{\frac{\Gamma_1 p}{\rho}} \quad (5)$$

where  $\Gamma_1$  is one of the adiabatic exponents. Assuming the star is an ideal gas, this equation can also be written in the form:

$$c = \sqrt{\frac{\Gamma_1 k_B T}{\mu m_u}} \quad (6)$$

where  $k_B$  is Boltzmann's constant,  $\mu$  is the mean molecular weight and  $m_u$  is the atomic mass unit. From these equations we can see that the sound speed within the stellar cavity has a dependency on pressure and density and consequently on temperature and chemical composition (Aerts et al., 2010).

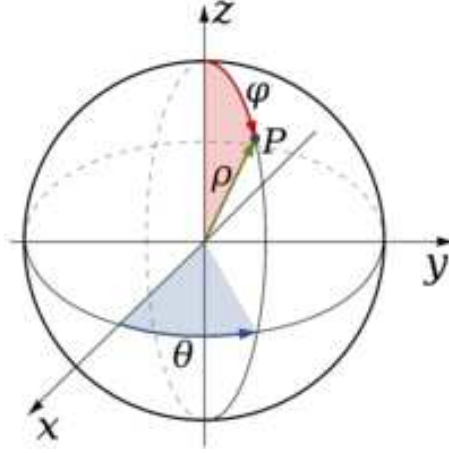


Figure 5: The spherical polar coordinate system.  $\rho$ ,  $\theta$  and  $\phi$  are the radial distance, co-latitude and longitude respectively. From [www.mathforum.org](http://www.mathforum.org)

As stars pulsate in three orthogonal directions, and in most cases can be considered spherical, they are best defined by a spherical polar coordinate system where  $\rho$ ,  $\theta$  and  $\phi$  are the radial distance, co-latitude and longitude respectively (see Fig. 5). As  $\theta$  is measured from the pole, it defines the pulsation pole or preferred axis. When considering a spherically symmetric star, the displacement due to pulsations is specified by the following spherical harmonic equations:

$$\xi_\rho(\rho, \theta, \phi, t) = a(\rho)Y_l^m(\theta, \phi)\exp(-i2\pi\nu t) \quad (7)$$

$$\xi_\theta(\rho, \theta, \phi, t) = b(\rho)\frac{\partial Y_l^m(\theta, \phi)}{\partial \theta}\exp(-i2\pi\nu t) \quad (8)$$

$$\xi_\phi(\rho, \theta, \phi, t) = \frac{b(\rho)}{\sin\theta}\frac{\partial Y_l^m(\theta, \phi)}{\partial \phi}\exp(-i2\pi\nu t) \quad (9)$$

where  $\xi_\rho$ ,  $\xi_\theta$ ,  $\xi_\phi$  are the displacements,  $a(\rho)$  and  $b(\rho)$  are the amplitudes,  $\nu$  is the oscillation frequency and  $Y_l^m(\theta, \phi)$  are the spherical harmonics given by:

$$Y_l^m(\theta, \phi) = (-1)^m \sqrt{\frac{2l+1(l-m)!}{4\pi(l+m)!}} P_l^m(\cos\theta)\exp(im\phi) \quad (10)$$

and  $P_l^m(\cos\theta)$  are Legendre polynomials given by:

$$P_l^m(\cos\theta) = \frac{1}{2^l l!} (1 - \cos^2\theta)^{m/2} \frac{d^{l+m}}{d\cos^{l+m}\theta} (\cos^2\theta - 1)^l \quad (11)$$

The number of radial nodes,  $n$  and is called the overtone of the mode,  $l$  is the degree of the mode and specifies the number of surface nodes, and  $m$  is the azimuthal order and specifies how many of the surface modes are lines of longitude. The values of  $m$  range from  $-l$  to  $+l$  which in turn generate  $2l+1$  modes (Aerts et al., 2010). The frequency of a mode depends on the sound travel time, thus the lower degree  $l$  modes penetrate more deeply and have lower frequencies. Furthermore, modes where  $m \neq 0$  are travelling waves where positive values of  $m$  are prograde and negative values of  $m$  are retrograde modes with respect to the rotation of the star.

Radial modes have the value  $l=0$ . If a  $\delta$  Scuti star pulsates simultaneously in the fundamental ( $n=0$ ) and first overtone ( $n=1$ ) radial modes, they can be identified by their period ratio of 0.77. This is a consequence of the sound speed variations as a function of temperature and chemical composition. For Cepheid variables, the observed ratio is less (0.71) due to their differing evolutionary states and hence interior structure and composition.

These variations can be detected as a change in the total observed flux or as a shift in the stellar spectrum caused by the expansion and contraction of the star. Through the equations of stellar structure and spherical harmonics, the period and amplitude of these fluctuations can be modelled to further understand the stellar interior.

## 1.6 Tidally Induced Pulsations

When two stellar components are in a binary system with an eccentric orbit, the interactions between the two components are variable dependent on phase. In some cases such interactions can cause the star or stars to oscillate. These oscillations are the result of the natural free eigenfrequencies of the star (theorised to be gravity modes of spherical degree  $l=2$ ) resonating with the dynamic tides (Aerts & Harmanec, 2004). The signatures of these interactions are frequencies that are multiples (harmonics) of the orbital frequency.

Further evidence of resonant pulsations is a second oscillation mode separated from such a harmonic by the rotational frequency of the star (Aerts & Harmanec, 2004). From a purely geometrical point of view, the occurrence of frequencies separated by the rotational frequency of a star happens because the pulsations occur in a reference frame (which can be defined by spherical polar co-ordinates  $r', \theta', \phi'$ ) that is rotating with respect to our own inertial frame of reference (which can be defined by spherical polar co-ordinates  $r, \theta, \phi$ ). The two frames of reference are related by the following expression:

$$(r', \theta', \phi') = (r, \theta, \phi - \Omega t) \quad (12)$$

where  $\Omega$  is the angular velocity and  $t$  is time. As the pulsation displacement vector depends on  $\cos(m\phi' - \omega_0 t)$  in our inertial frame of reference it therefore depends on  $\cos(m\phi - \omega_m t)$  where  $\omega_m = \omega_0 + m\Omega$  and  $m$  is the azimuthal order of the mode (Aerts et al., 2010). In reality, these values deviate from the absolute values due to the Coriolis force and surface convection currents. However, it can be seen that for any true mode where  $m \geq 1$ , rotational splitting will occur in multiplets in accordance with  $m$ . If

such a multiplet occurs where one of the dominant peaks is an orbital harmonic, this is evidence that the frequency is indeed a true pulsation and not a result of data manipulation (for example a bad model fit).

It has been suggested by Reed & Brondel (2005) that it is possible for tidal interactions to exert a greater force on the stellar components than the Coriolis force. In such a case the pulsation axis of the star is expected to be directed towards its binary companion, not along the axis of rotation as generally assumed. This theory is called the Tidal Locking Hypothesis and is a result of the minimum energy formation being assumed by the system. This arrangement has not yet been observed, although a similar situation exists with rapidly oscillating Ap (roAp) stars where the pulsation axis is aligned with the magnetic field of the stellar component (Kurtz, 1982). The identifier for tidal locking is a frequency spectrum containing multiplets separated by the orbital frequency. Other implications for binaries with tidally excited modes include the possibility of determining the orbital inclination from the shape of the stellar light curve. Kumar et al. (1995) demonstrated how variations in inclination generate specific signatures in the light curve, which can be attributed to the  $l=2$  mode.

It has also been acknowledged that objects with tidally resonant pulsations may no longer be described by the classical apsidal motion formula (see eq.3). Quataert et al. (1995) demonstrated that in the case of modes where the ratio of the pulsation frequency and the orbital frequency is less than 7, deviation from the classical apsidal motion formula occurs; such phenomena are now being observed on a regular basis with the high precision data obtained by satellites such as *Kepler*.

## 1.7 Kepler Mission

The *Kepler* satellite (Borucki et al., 2010; Gilliland et al., 2010), with its highly precise photometric CCD, is generating observations unparalleled in detail and subsequently giving greater insight into the study of stellar structure through the use of asteroseismology. The primary objective of the *Kepler* mission is the identification and classification of planets through the transit method (Gilliland et al., 2010). However, the instrumentation required for such observations is highly applicable to the field of asteroseismology. Attributes, such as a stable platform, that enable extended observations, and a precision of 1 part per million make the *Kepler* observations quintessential for the advancement of asteroseismology. A dynamic range of over a factor of 10 000 in apparent brightness, in addition to a  $105 \text{ deg}^2$  field of view, give *Kepler* an unprecedented advantage for achieving the best quality asteroseismic data. Moreover, the ability to generate short cadence data of approximately 1 min, allows for the detailed photometric analysis of pulsating stars across the H-R diagram.

The *Kepler* satellite, which is depicted in Fig. 6, has a 1.4-m primary mirror (Kjeldsen et al., 2010) and is in an Earth trailing heliocentric orbit. It has 41 fully functional CCDs (originally 42), with  $2000 \times 1000$  pixels each  $4 \times 4$  arcseconds, which can observe up to 150 000 stars at any given time. The telescope points towards the constellations Cygnus and Lyra in an orientation that avoids the brightest stars, which would saturate the CCD pixels. Data are transmitted to Earth once a month via the Deep Space Network to the Mission Operations Centre (Jenkins et al., 2010). Upon the culmination of each quarter the space craft performs a roll to realign the solar panels and CCDs in the correct orientation. During this period the *Kepler* satellite does not acquire data yet still obtains an extraordinarily high duty cycle in comparison to other observational techniques.

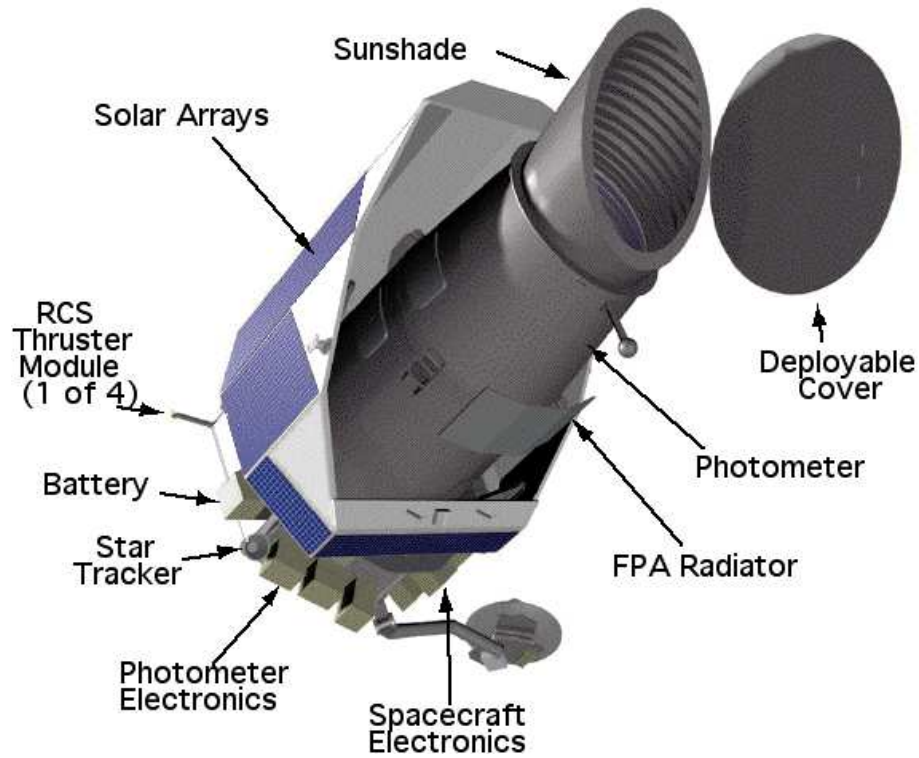


Figure 6: A schematic drawing of the *Kepler* Space Craft. Here you can see the position of the solar arrays which require realignment once per quarter of a *Kepler* orbit. The photometer is directed towards the constellations Cygnus and Lyra. From [www.astro.wisc.edu](http://www.astro.wisc.edu).

The *Kepler* data are disseminated to several groups to be examined for planetary transits, asteroseismic purposes, binary star science, spots and flares. The purpose of the Kepler Asteroseismic Science Consortium (hereafter KASC) is the asteroseismic investigation of objects identified by *Kepler*. Furthermore, the main objectives, as specified in the KASC documents, are: the determination of the radii and masses of stars that host planets; to distinguish between main sequence and evolved stars with host planets; and the general asteroseismic investigation of stellar parameters.

The data provided by the Kepler Asteroseismic Science Operations Center (hereafter KASOC), which are run by KASC, are time stamped with Truncated Barycentric Julian date, which is Barycentric Julian date - 2400000. Temperatures are provided for each object, which are determined through photometry using SDSS, 2MASS and KeplerCam on the 48-inch telescope at the Whipple Observatory on Mount Hopkins, Arizona (Latham et al., 2005). RA and Dec, and estimates of  $\log g$ , radius, metallicities and magnitudes of the objects are also provided with each data set, combined with a contamination estimate, which indicates the amount of contaminant light that is incident from other objects in the mask.

## 2 Observations of KIC 4544587

KIC 4544587 is an eccentric ( $e = 0.28375 \pm 0.00005$ ), short-period binary system of magnitude  $K_p = 10.8$  (where  $K_p$  stands for the *Kepler* band pass magnitude). The *Kepler* band pass, which is essentially a white light broadband filter, includes the the g-r-i-z filter sequence consistent with the Sloan Digital Sky Survey. KIC 4544587 is in the constellation Lyra at a distance of approximately 1.7 kpc; other identifiers for this object can be found in Table 1. The primary component is an early A star that is within the  $\delta$  Scuti instability strip and the secondary component is an early G star, which is likely to be a solar type oscillator, although no solar-like oscillations have been identified in our data. It is also likely that the primary component is a metallic-lined, Am star, presuming that through tidal interactions the equatorial rotation rate is  $v_{equ} < 120 \text{ km s}^{-1}$ , which is slow enough for diffusion to occur (Abt, 2009).

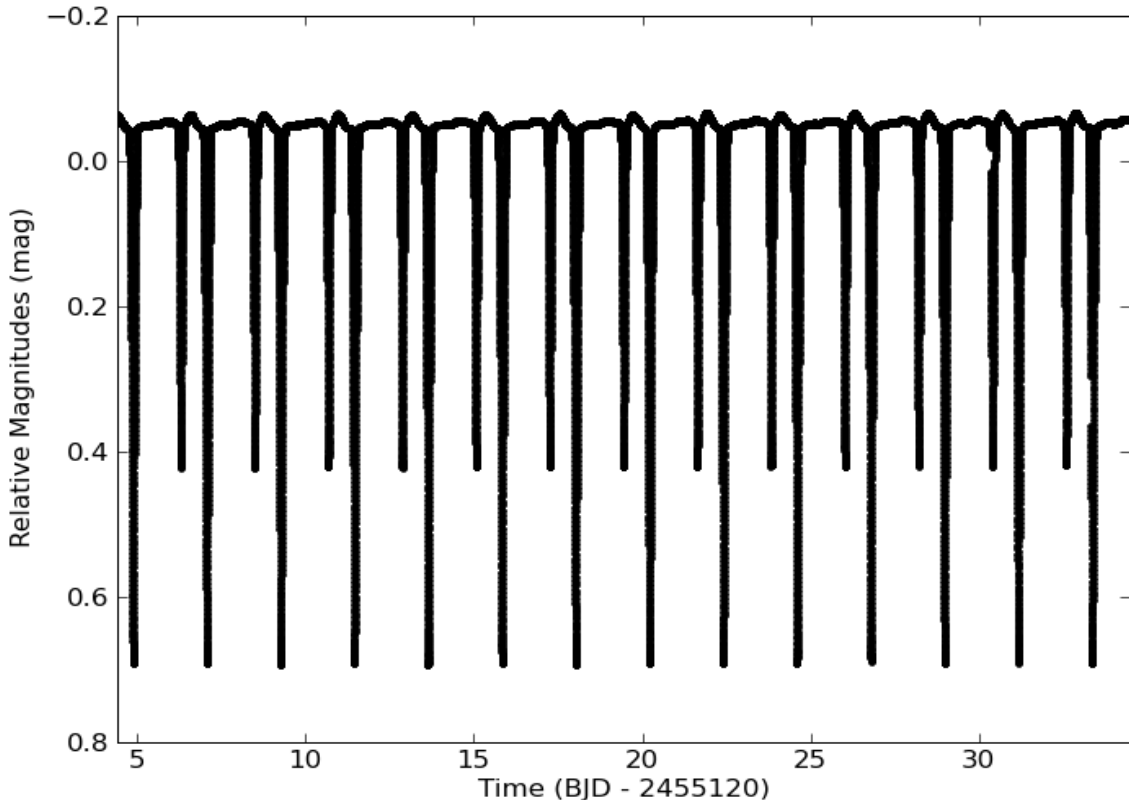


Figure 7: The total observed *Kepler*, short cadence light curve from Quarter 3.2.

Primarily this object was selected as a likely candidate for tidally enhanced pulsations due to the close proximity of the components ( $\sim 8 R_{\odot}$ ) at periastron. When considering the radius of each stellar component, this suggests that the distance between the stellar surfaces at periastron is  $\sim 5 R_{\odot}$ . Secondly, as the system contains a  $\delta$  Scuti star, KIC 4544587 is rich in asteroseismic information. KIC 4544587 also has interesting orbital characteristics, which include a hump in the *Kepler* photometric light curve after secondary minimum that is due to stellar distortion and reflection effects. Such a feature is indicative of an eccentric binary with its components in close proximity to each other (Maceroni et al., 2009).

The *Kepler* photometric observations of KIC 4544587 consist of both long cadence (hereafter LC) data, during Quarters 0, 1 and 6, and short cadence (hereafter SC) data during Quarters 3.2 and 7

Table 1: Other identifiers and basic data for KIC 4544587. The *Kepler* magnitude (Kp) specified is derived from the *Kepler* broadband filter.

Identifiers	
TYC	3124-1348-1
GSC	03124-01348
2MASS	J19033272+3941003
Observable Information	
RA (2000)	19:03:32.7274
Dec (2000)	+39:41:00.314
<i>V</i>	10.8
<i>B</i>	10.89
Kp	10.80

Table 2: Information on the data acquired for each Quarter. The long cadence data (LC) corresponds to a sampling rate of 29.4244 min and short cadence data (SC) to a sampling rate of 58.8488 s.

Quarter	Cadence	Number of data points	Duty cycle
0	LC	476	99.5%
1	LC	1 639	98.1%
3.2	SC	44 000	99.5%
6	LC	4 397	97.2%
7	SC	128 830	98.9%

(see Table 2). A Quarter is defined as a quarter of a complete, 372.5 d, *Kepler* orbit around the Sun (Kjeldsen et al., 2010). LC data correspond to a sampling rate of 29.4244 min and SC data to a sampling rate of 58.8488 s. For both formats 6.02 s exposures are co-added on board; this occurs 270 times to form an LC data point and 9 times to form an SC data point (Caldwell et al., 2010); the data are then time-stamped with Truncated Barycentric Julian Date (Gilliland et al., 2010). The observations of KIC 4544587 span from 2009 May to 2011 May and comprise 179 342 data points. Of these 476, 1 639 and 4 397 LC data points were obtained in Quarters 0, 1 and 6 respectively and 44 000 and 128 830 SC data points in Quarters 3.2 and 7. Fig. 7 depicts the Quarter 3.2 SC light curve and Fig. 8 is an enlarged section demonstrating the ellipsoidal and pulsational variability intrinsic to the system.

From the total data set 1569 points were removed as outliers, of which 214 data points were removed from Quarter 3.2 and 1207 from Quarter 7. These outliers were selected by eye as the intrinsic variations in the data significantly reduce the effectiveness of automated sigma clipping. Cosmic rays and brightening events known as Argabrightening, named after the discoverer, V. Argabright (Van Cleve, 2009), are the dominant cause of outliers. Small gaps in the data are also present due to safe mode events and spacecraft rolls. These effects, however, are minimal, which can be seen by the high duty cycle that was obtained for each Quarter independently (see Table 2). For Quarter 3.2 the raw flux data, converted into relative magnitudes, were used during the data analysis. The instrumental effects were removed from the data using an 8<sup>th</sup> order polynomial as discussed in § 4.4.1. For Quarter 7 the raw flux

data were used during analysis, which were detrended using sigclip as discussed in §4.5.1.

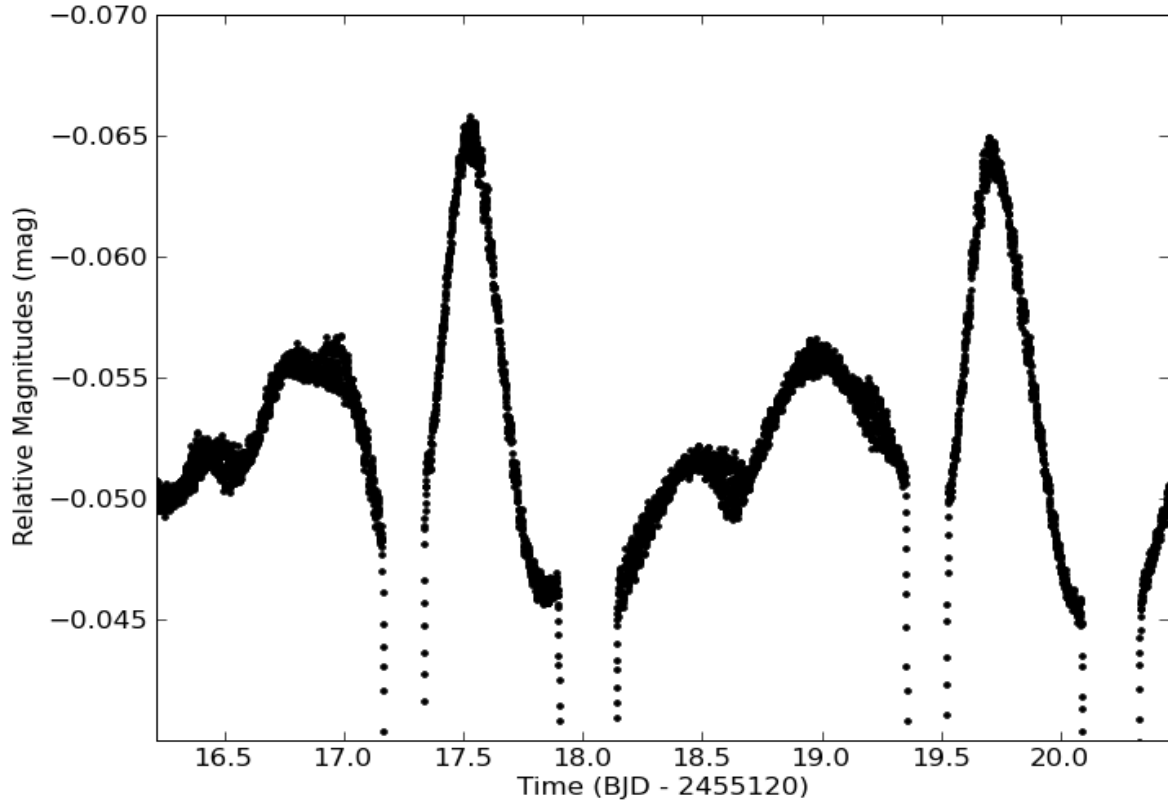


Figure 8: An amplified image of a section of the *Kepler* short cadence light curve. Here the dominant pulsation modes and the hump between primary and secondary minima are clearly visible. (The first of these is centred on 17.5 BJD - 2455120).

The contamination value for KIC 4544587, specified by the Kepler Asteroseismic Science Operations Center (KASOC), is estimated to be 0.019, where 0 implies no contamination and 1 implies complete contamination of the CCD mask. This contamination value suggests that 98.1 per cent of the total light observed is intrinsic to KIC 4544587. Even though the value of 0.019 is low, it is still possible that variability from an external source could affect the flux and hence the frequency spectrum of KIC 4544587. However, we see no evidence for this in the *Kepler* light curve or frequency spectrum. (Future spectroscopic observations will attempt to confirm this).

### 3 Identification of the Orbital Period

Period analysis was performed to identify the orbital period of the KIC 4544587. An initial estimate was obtained by applying PERIOD04 (Lenz & Breger, 2004) to the SC data from Quarter 3.2 only. PERIOD04 applies a Fourier transform to the data and uses least squares fitting to ensure the amplitudes and phases are calculated simultaneously. Further analysis was then performed on the total data set using the phase dispersion minimisation (PDM) technique (Stellingwerf, 1978). A complete discussion of the application of PDM to the data and the results obtained can be found in § 3.1.

Subsequently, to test the PDM software, JKTEBOP (Southworth et al., 2004a; Southworth, 2008) was applied to the SC data of Quarter 3.2 and Quarter 7. JKTEBOP is based on the EBOP light curve modelling program, where EBOP is an acronym for ‘Eclipsing Binary Orbit Program’ (Etzzel, 1981; Popper, 1984). EBOP has been updated by Southworth et al. (2004a), formally known as John Kevin Taylor, who subsequently added his initials, JKT, as a prefix. For Quarters 3.2 and 7 the period found using JKTEBOP agreed with that found using the PDM technique to an accuracy of  $4\sigma$ . Following further analysis an inconsistency between the two data sets was attributed to apsidal motion, which is discussed in § 4.5.3. JKTEBOP was well-suited to this task as it is extremely efficient at analysing large quantities of precise data on account of its low numerical noise. Using JKTEBOP, for Quarter 3.2 we obtained an orbital ephemeris of:

$$\text{MinI} = \text{BJD } 2455124.885160(5) + 2.1891084(11) \times E$$

and for Quarter 7 we obtained an orbital ephemeris of:

$$\text{MinI} = \text{BJD } 2455124.85280(6) + 2.1891134(44) \times E$$

where MinI corresponds to the time of primary minimum and the values in the parentheses give the  $1\sigma$  uncertainty in the previous digits. This demonstrates that although the periods are the same to an accuracy of  $1\sigma$ , the true difference has generated an off set in the zero points.

#### 3.1 Phase Dispersion Minimisation

Phase dispersion minimisation (PDM) is a method used for finding the period of data when the data are not evenly sampled, have large gaps or are non-sinusoidal, such as binary light curves (Stellingwerf, 1978). As KIC 4544587 was not selected to be observed during Quarters 2 or 5, gaps in the data occur during these times. Further gaps also appear in the data set due to safe mode events and the transmission of data at the end of each quarter. Moreover, the features in the data are not specifically sinusoidal, and hence PDM is highly suited to finding the orbital period of KIC 4544587. I created a piece of software after Stellingwerf (1978) to find the orbital period of KIC 4544587, for which the details are as follows. When applying the PDM technique to the total data set, to avoid weighting by the number of data points, all SC data were converted to LC. The PDM technique was then repeated on the SC data of Quarters 3.2 and 7 separately.

To generate the period using PDM, initially the variance is calculated for the whole data set:

$$\sigma^2 = \frac{\sum(x_i - \bar{x})^2}{N - 1} \quad (13)$$

where  $x$  is the magnitude at each time point  $t$  and  $N$  is the number of values (where  $i = 1, N$ ).

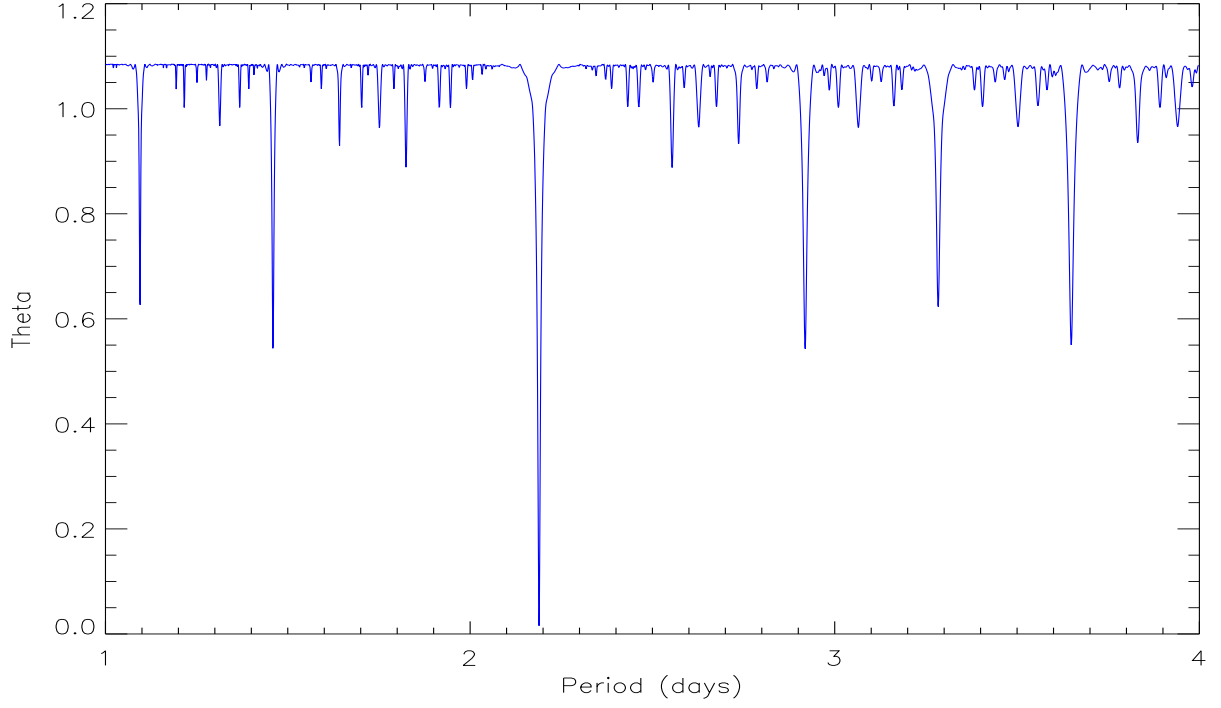


Figure 9: A graph demonstrating  $\Theta$  as a function of period using 100 bins and a precision of 0.0001 on the Quarter 7 data. Statistically  $2.1891 \pm 0.00005$  d is the most significant period in the data between 1 d and 4 d.

Following this  $\Theta$ , which is the ratio of the variance of the phase binned data to the variance of the total data set, was calculated for the range of periods that is specified by the user. Starting with the shortest period in the range, the data are converted from the time domain to the phase domain:

$$\phi_i = t_i/\Pi - [t_i/\Pi] \quad (14)$$

where  $\phi$  is the phase,  $t$  is the time,  $\Pi$  is the period and the square brackets denote the integer part of the value. The data are then arranged in ascending order of phase and separated into bins. The number of bins is specified by the user and is denoted  $M$ . The variance of the binned data,  $s_j^2$  where ( $j = 1, M$ ), is then calculated for each bin using eq. 13.

The variance of all  $M$  samples can then be calculated for the given period by:

$$s^2 = \frac{\sum (n_j - 1) s_j^2}{\sum n_j - M} \quad (15)$$

where the variance of each bin gives a measure of the scatter around the mean light curve. The value  $s^2$  is a measure of the bin variance for the overall data set. Theta is then calculated, where  $\Theta$  is the ratio of the variance of the total data set to the variance of the binned data arranged by phase:

$$\Theta = s^2/\sigma^2 \quad (16)$$

This process is repeated for all periods within the specified range incremented by the user-specified precision. The value for  $\Theta$  will be approximately equal to 1 when  $\Pi$  is not a correct period. As a

Table 3: The period, frequency and corresponding  $\Theta$  values generated by the phase dispersion minimisation software. The various values have been generated by altering the bin size and precision value, the precision value used was 0.0000001. The slight difference between the values is consistent with that found with JKTEBOP and thus is attributed to apsidal motion. The uncertainty in the period is  $\pm 5$  following the final digit specified and in the uncertainty in the frequency is  $\pm 1$  following the final digit specified.

Quarter	Bins	Period (d)	Frequency ( $\text{d}^{-1}$ )	$\Theta$
Q 3	150	2.1891142	0.45680577	0.011427
Q 7	300	2.1891122	0.45680618	0.005365
Complete data set	150	2.1891101	0.45680661	0.032712

significant period is approached there is a reduction in the value of  $\Theta$ , this can pertain to a real peak, harmonic or alias. The minimum value of  $\Theta$  corresponds to the most significant period (see Fig. 9).

As the data sets are large, only the theta test is required to calculate the significance of the peak (Stellingwerf, 2010). Furthermore, the F test, which is a standard test for comparing statistical models, is no longer considered appropriate for statistical application to PDM. This is because the phase dispersion minimization technique does not closely follow the F distribution (also known as the Fisher-Snedecor distribution) because the two variables,  $s$  and  $\sigma$ , are not independent, and thus is not sensitive to it (Schwarzenberg-Czerny, 1989).

The method for deriving  $s$  and hence  $\Theta$  is such that if the number of bins,  $M$ , is greater than the number of data points per bin,  $n_j$ , then  $\Theta$  becomes negative. Subsequently, in Table 3, the maximum number of bins is 150 for Quarter 3.2 and for the total data set in long cadence, where as for Quarter 7 it is increased to 300 due to the increased number of data points.

It is evident from the  $\Theta$  values that  $2.18911 \pm 0.00005 \text{ d}^{-1}$  is a correct value for the period for both the Quarter 3.2 data and the Quarter 7 data. However, to a greater level of significance the values are not consistent with each other. The discrepancy between the Quarter 3.2 and Quarter 7 values is  $(1.04 \pm 0.07) \times 10^{-6}$ , which although small, was significant enough to further investigate the possibility of apsidal motion. If the system is undergoing apsidal motion we would expect a change in the anomalous period, which is the time elapsed between consecutive primary eclipses; essentially what the PDM method is measuring. In a system that demonstrates apsidal motion the anomalous period is not equal to the true period as both eclipses are moving relative to each other, and so neither is fixed with respect to a single orbit. Further discussion on apsidal motion and the anomalous period can be found in § 4.5.3.

## 4 Binary Modelling

The purpose of binary modelling is to generate a set of fundamental parameters through the consideration of photometric and radial velocity curves. The binary modelling programs currently available require initial estimates of specific binary parameters from which a model is generated. These parameters can include: theoretically defined values such as albedos and gravity brightening exponents; spectroscopically determined values including temperature,  $\log g$  and metallicity; and photometrically determined values such as relative flux values and relative radii.

Tightly constrained parameters, such as those observationally or theoretically determined, are held fixed during the fitting process as this reduces the number of free parameters and hence the number of dimensions in parameter space. The modelling program then alters the fitted parameters simultaneously to generate a model that is consistent with the observed data. The three modelling programs considered here are JKTEBOP (Southworth et al., 2004a; Southworth, 2008; Etzel, 1981; Popper, 1984), the Wilson-Devinney code (Wilson & Devinney, 1971; Wilson, 1979; Wilson & Van Hamme, 2004) and PHOEBE (Prša & Zwitter, 2005); where PHOEBE is based on the Wilson-Devinney code but contains several improvements as discussed in §4.5.

The analysis of a photometric light curve alone will not generate accurate values of the fundamental parameters. This is for two reasons: there is not enough information in a photometric light curve to determine absolute properties (for example the absolute radii and the semi-major axis); and there is a degeneracy that occurs due to the correlations between the parameters. For example, the potential of the secondary is highly correlated with the mass ratio and both the potentials are highly correlated with the inclination. Moreover, there is not enough information in a photometric light curve to determine the absolute dimensions of the orbital dynamics. For this reason it is highly advantageous to combine photometric data with spectroscopic data in the form of radial velocity curves, although this does not guarantee that the global minimum will be identified. Currently the analysis of KIC 4544587 is dependent on photometric data only. However, future work will include the analysis of this object using both light and radial velocity curves.

In an attempt to avoid local minima and to estimate errors correctly, two options are available: once a solution is reached the parameters should be perturbed by a user defined value (commonly 10%) to identify the parameter correlations (a method known as parameter kicking); and by implementing heuristic scanning such as a Monte Carlo simulation (hereafter MC). Using both these methods the most likely parameter values can be identified with the corresponding statistical error estimates. Currently only the formal errors have been calculated for KIC 4544587. However, future work will include the identification of the uncertainties involved using a combination of MC and parameter kicking.

The SC data of Quarter 3.2 and Quarter 7, were used in the subsequent modelling and mode identification of KIC 4544587. The SC data have the advantage of increased time resolution which enables the identification of the p mode pulsations that are present in this object. As the *Kepler* data are released on a quarterly basis, the data of Quarter 7 are only a recent addition to the total data set and consequently the analysis is incomplete. However, the Quarter 3.2 data were obtained prior to the commencement of this project and so have undergone thorough analysis.

All data were used, ranging from Quarter 0 to Quarter 7 in the determination of the rate of apsidal advance. The rate of apsidal advance is a measure of the precession of the line of apsides as a function

of time. The increased time coverage was necessary to tightly constrain this effect (see § 4.5.3).

## 4.1 Binary model parameters

The current binary modelling programs are based on Roche lobe geometry. Within this geometry each stellar component is classified as a point mass with an instantaneous equipotential surface. The shape of the surface of each component is defined by the potentials of the primary and secondary components and the centrifugal force of the binary system. The potentials are a combination of the gravitational forces and the pressure gradient, as a function of radius (Prša, 2005). The Roche model assumes that each stellar component is a rigid body that rotates uniformly about its axis and that any perturbations to the equipotential shape, such as oscillations, are negligible (for this reason the pulsations are prewhitened, prior to the generation of a final model, as discussed in § 4.3.2).

Each of the binary modelling parameters not only has a definition, but also a set of considerations that need to be acknowledged when modelling a binary system. Fundamentally these parameters are as follows (although it is often the case that a combination of parameters is used for implementation purposes):

### Potentials

The potentials of the stars are dimensionless quantities that define the shape and characteristics of each star within the Roche model. Wilson (1979) adapted Kopal’s Law, which defines the potentials of the stellar components, to include the instantaneous separation, thus enabling the determination of the varying potentials at each phase for an eccentric, asynchronous orbit:

$$\Omega = \frac{1}{r} + q \left[ \frac{1}{\sqrt{d^2 - 2\lambda dr + r^2}} - \frac{\lambda r}{d^2} \right] + \frac{1}{2} F^2 (q + 1) r^2 (1 - \nu^2) \quad (17)$$

where  $\Omega$  is the potential of the stellar component at a particular phase,  $r$  is the radius relative to the semi-major axis,  $q$  is the mass ratio of the system,  $d$  is the instantaneous separation,  $F$  is the stellar angular rotation rate relative to the orbital rotation and  $\lambda$  and  $\nu$  are the direction cosines which evolve from the use of spherical coordinates:  $x = r \sin \theta \cos \phi = \lambda r$  and  $z = r \cos \theta = \nu r$ .

The potential is used as a proxy for the inverse radius. Considerations towards the physical nature of this parameter must be made, since if the potential is too large then the physical equivalent is a star with a hole in the back. Also, small potentials are indicative of a component undergoing Roche overflow generating either a semi-detached or over-contact system. Furthermore the potential of the secondary star is derived from the potential of the primary, as a function of the mass ratio (through an inversion of eq 17). For this reason the mass ratio and potentials are highly correlated and so should not be fitted simultaneously.

### Mass Ratio

There is not a large amount of information pertaining to the mass ratio in a photometric light curve. The masses of the components are evident at quarter phases as ellipsoidal variations and periastron brightenings, and during ingress and egress if the components are heavily distorted, for example in a semi-detached or over-contact binary system. This is because the stellar distortion, which is evident in the light curve during ingress and egress, depends on the radii of the components (as a function of

the semi-major axis), the mass ratio, the instantaneous separation and the synchronicity parameter. Consequently, in a system that demonstrates extreme ellipsoidal variations, by fitting the mass ratio and potentials the photometric mass ratio can be acquired.

The most pertinent way to determine the mass of the two stellar components is through double-lined spectra: with accurate radial velocity curves, the mass of the components of a stellar system can be obtained to an accuracy of 1% (Torres et al., 2010).

## Temperature

As it is a directly measurable quantity through observed spectra; the effective temperature is incorporated into the modelling process. Even though the individual temperatures of the stellar components cannot be uniquely identified using the light curve alone, the temperature ratio is tightly constrained. If the temperature is coupled with the luminosity, the luminosity of the secondary component is determined from the temperature ratio. This is done using the Stefan-Boltzmann law:

$$L \propto R^2 T^4 \quad (18)$$

where  $L$  is the stellar luminosity,  $R$  is the radius and  $T$  is the effective temperature. The effective temperature is a global parameter, but as the temperature of a star is not uniform over the stellar surface, gravity brightening and limb darkening laws are incorporated to obtain the local surface luminosity as a function of temperature.

## Luminosity

The luminosities of the stellar components are not tightly constrained during the modelling process (unless the photometric light curve is in multiple pass bands), however, the ratio of the stellar surface brightnesses is very well constrained by the ratio of the depths of the eclipses. Furthermore, for a total, flat bottomed eclipse, the ratio of the light lost to the light remaining equals the ratio of the luminosity of the smaller to the larger star. Within the WD code the light contributions of the primary and secondary components, HLUM and CLUM (called so due to the hot and cold star identities that originally defined the stellar components), are arbitrary, based on the input light curve. These parameters determine the level and scale of the synthetic model light curve. The luminosity over the complete stellar surface is specified as  $4\pi$  times the flux per steradian.

## Gravity Brightening

Gravity brightening occurs when the rotation and tidal deformation of a star causes it to deviate from spherical shape into an oblate spheroid. The oblateness generates a variation in brightness due to the varying gravitational acceleration across the stellar surface:

$$F \propto F_{pole} \left( \frac{g}{g_{pole}} \right)^\beta \quad (19)$$

where  $F$  is the flux,  $g$  is the gravitational acceleration and  $\beta$  is the gravity brightening exponent. As the star rotates, the stellar poles experience a greater amount of gravitational acceleration, leading to an increase in the local temperature, whereas at the equator the surface extends away from the star and

thus becomes cooler. The values for  $\beta$  have been derived theoretically for stars in radiative equilibrium by von Zeipel (1924) for the radiative case ( $\beta = 1$ ) and empirically by Lucy (1967) for the convective case ( $\beta = 0.32$ ).

### Limb-Darkening Coefficients

Limb-darkening describes the apparent brightness variation across the stellar surface from centre to limb. As we observe the edge of the stellar disk, although our line of sight penetrates to the same optical depth, it does not penetrate to the same geometric depth as at the centre. For this reason the stellar surface appears brighter at the centre than at the edges (see Fig. 10).

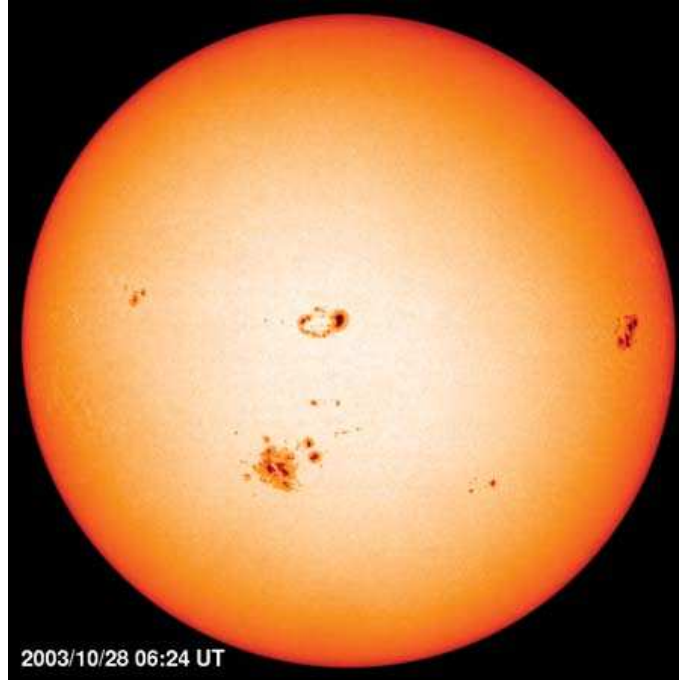


Figure 10: An image of the Sun that demonstrates the variation of the light from center to limb due to limb darkening. The observations were performed by the Solar and Heliospheric Observatory satellite, 2003 Oct. 28. From [www.britannica.com](http://www.britannica.com)

The effect of limb darkening on local surface brightness is incorporated into the modelling process to describe the variation of light as a function of distance from the centre of the stellar disk. The standard function that describes this intensity transition is the linear function (see eq. 20). However, this function has been adapted into a square root (Klinglesmith & Sobieski, 1970) function (see eq. 21), which is applicable to stars of  $T_{\text{eff}} > 9000$  K and a logarithmic (Diaz-Cordoves & Gimenez, 1992) function (see eq. 22), which is applicable to stars of  $T_{\text{eff}} < 9000$  K when observing in the optical (Prša, 2005):

$$L(\varphi) = 1 - x_\lambda + x_\lambda \cos \varphi \quad (20)$$

$$L(\varphi) = 1 - x_\lambda + x_\lambda \cos \varphi - y_\lambda(1 - \sqrt{\cos \varphi}) \quad (21)$$

$$L(\varphi) = 1 - x_\lambda + x_\lambda \cos \varphi - y_\lambda \cos \varphi \log(\cos \varphi) \quad (22)$$

where  $L(\varphi)$  is the luminosity as a function of position expressed in terms of the luminosity at the centre of the stellar disk and  $x_\lambda$  and  $y_\lambda$  are wavelength dependent limb darkening coefficients.

## **log g**

The gravitational acceleration experienced by a test particle at the stellar surface is expressed by the global parameter  $g$ .  $\log g$  is specified in cgs units and is a proxy for the size of the star, thus it does not include consideration of variations that occur on the micro scale.  $\log g$  is an observed parameter and can be identified in the shape of spectral lines.  $\log g \sim 4.0$  and  $\log g \sim 2.5$  are values indicative of a main sequence star and red giant respectively.

## **Albedo**

The albedo is a measure of the light incident from the companion star that is re-radiated away from the stellar surface. Consequently, a star with a fully radiative envelope has an albedo of 1.0 (Eddington, 1926; Milne, 1926) which equates to 100% of the light being radiated away. For a star with a convective surface, however, approximately 50% of the emergent light is reabsorbed, thus the theoretical value for the albedo is between 0.4 and 0.5 (Ruciński, 1969), the uncertainty of which is due to the uncertainty in the mixing length scale factor. The most prominent effect of the albedo can be seen on the shoulders of the minima.

Claret (2001) determined that the upper temperature limit, where a star's envelope should be defined as convective for the purpose of the albedo and gravity brightening exponent, is  $\sim 6300$  K. This is because at this temperature the convective envelope is thin enough that it does not play an important role in these effects. However, Claret (2001) also suggests that, with the advent of improved observations using satellites, the uncertainty in the albedo is likely to pose a problem.

## **Multiple Reflection**

Reflection effects are considered globally through the albedo parameter. However, within some modelling programs, such as WD and PHOEBE, multiple reflection effects are considered. This function determines how the reflection (re-radiation) of heat from one star affects the temperature distribution on its companion; this becomes highly important for hot dense stars such as subdwarf B stars and white dwarfs where a multiple number of reflections need to be considered. These effects occur on small scales and are most prominent on the area of the star that is directed towards its companion and hence are not defined by the albedo alone.

## **Time of Primary Minimum and Phase Zero**

The traditional definition for the time of primary minimum and zero phase is the time where the primary star (defined as the hotter star) is being eclipsed by the secondary star. For a system in a circular orbit or system where the longitude of periastron is equal to  $\pi/2$  rad, the time of superior conjunction also coincides with phase zero. However, due to apsidal motion, it is often required that phase zero is defined separately from the time of superior conjunction for an eccentric system. In this case the time of phase zero is defined as the far intersection of the line of sight along a node that is central to the ellipse of the orbit (see Fig. 11).

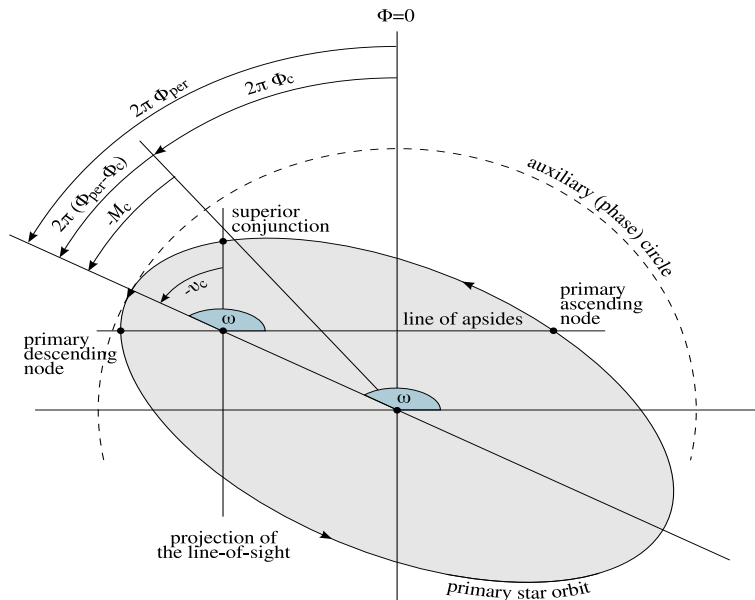


Figure 11: An image demonstrating the orbital plane of the primary star. Here you can see the relation of phase zero and time of primary minimum. Phase zero is the far intersection of the line of sight along the node that is central to the primary orbit and time of primary minimum occurs when the primary star is at superior conjunction. From PHOEBE Scientific Reference (Prša & Zwitter, 2005).

## Phase Shift

The phase shift is the separation from the time of primary minimum to zero phase. This value is incorporated for convenience, as it is often preferable to specify the zero point in time as the time of primary minimum. Thus, the phase shift signifies the separation between primary minimum and the time of zero phase in terms of phase.

## Period

The sidereal period of a binary system is the time of one complete orbit from phase zero to phase zero (where phase zero is defined separately from the time of superior conjunction as specified above). If the traditional phase zero were considered here, in an eccentric binary system the period would be equivalent to the anomalous period which is discussed in section §4.5.3. The anomalous period varies with time as the line of apsides processes around the orbit causing the eclipse phases to vary with respect to each other.

## Semi-Major Axis

The major axis is defined as the line that passes through the two foci of the ellipse and is the longest axis of an elliptical orbit. (This reduces to the orbital diameter for a circular system.) The semi-major axis ( $a$ ) is half this quantity. When modelling radial velocity curves, by setting the inclination ( $i$ ) to  $90^\circ$ ,  $a \sin i$  and hence  $a$  can be accurately obtained. By then determining the inclination of the orbit through modelling, an accurate estimate of  $a$  may be acquired that is consistent with the orbital shape.

## Argument of Periastron

The argument of periastron,  $\omega$ , is the angle from the ascending node to the point of periastron (the point of closest approach). The line of nodes is the intersection between the plane of the orbit and

the tangential plane of the sky, and the ascending node is where the primary component passes from negative to positive inclination with respect to the tangential plane (see Fig. 12).

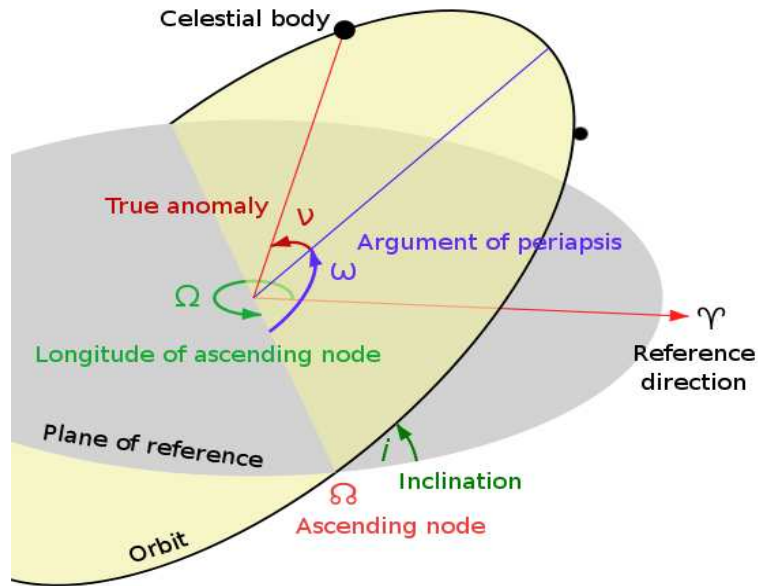


Figure 12: An image demonstrating the various parameters that define the orbital dynamics of a binary star system. The argument of periastron (or periapsis as specified here) is the angle measured from the ascending node to the point of periastron. From [www.uvs-model.com](http://www.uvs-model.com)

The radial eccentricity projection and the tangential eccentricity projection are described by a combination of the eccentricity and the argument of periastron. The ratio of the primary and secondary eclipse widths is determined by the tangential eccentricity projection,  $e \cos \omega$ . The radial eccentricity projection,  $e \sin \omega$ , determines the phase separation between the two eclipses and the shape of the eclipses (Prša & Zwitter, 2005).

### Inclination

The inclination of a system refers to its orientation of the orbit with respect to the plane of the sky. At  $90^\circ$  the orbit is perpendicular to the plane of the sky and at  $0^\circ$  the orbit lies in the plane of the sky. If an orbit is at any angle other than  $0^\circ$  it has an ascending and descending node.

### Eccentricity

All close binary systems tend towards either a synchronous circular orbit, or the two components eventually merge (Hut, 1981). However, as this is a generally slow process, many binary orbits are eccentric. Eccentricity has multiple influencing factors on the computation of the stellar parameters. Primarily it determines the magnitude of the variation of the gravitational forces exerted on each stellar component as a function of time. This has many consequences including: the requirement of a factor that denotes the instantaneous separation when calculating the potentials and hence shapes of the stellar components; the occurrence of a phase shift between zero phase and primary conjunction - although this can be zero when the line of apsides coincides with the line of sight (Kallrath, 2009); effects on the rotational synchronicity of the stellar components leading to tidal interactions (see §5.2) and hence apsidal motion; and it determines the width of the minimum that is closest to apastron in the light curve.

## 4.2 JKTEBOP

EBOP (Eclipsing Binary Orbit Program) is a binary modelling program that was created by Etzel (Etzel, 1981; Popper, 1984) based on models by Nelson (Nelson & Davis, 1972). It incorporates linear least squares fitting to model stellar light curves. This is done by calculating the intensity ratio at the centre of each stellar disk and approximating it to flux values using limb-darkening coefficients. From the best-fit model the stellar parameters are initially derived for spherical components. These values are then perturbed to allow for oblateness (Popper & Etzel, 1981). Due to the approximation that the stars are spheroids, EBOP is only applicable to detached systems where the individual components are approximately spherical, which encompasses all stars of oblateness less than 0.04 (Popper & Etzel, 1981). The analytical nature of EBOP makes it extremely efficient at analysing large quantities of precise data on account of its low numerical noise caused by inconsistencies in precision.

JKTEBOP is an updated version of EBOP that incorporates the Levenberg-Marquardt minimization algorithm to perform a linear least squares fit to the data (Southworth et al., 2005). Furthermore, the EBOP program has been modified to solve for both the sum and ratio of the radii of the stellar components and to perform automatic iterations. In each case the units are defined in a dimensionless manner and so do not depend on knowing the distance of the star.

### 4.2.1 Implementation of JKTEBOP to KIC 4544587

As JKTEBOP only allows for a maximum oblateness of 4%, it was not able to model the ellipsoidal nature of KIC 4544587. For this reason the residuals of the fit contain a large hump pertaining to the ellipsoidal variability in the system after secondary minimum. This can be seen in Fig. 13.

As stated in §3, JKTEBOP was initially used to determine the orbital ephemeris of the system. However, it was also incorporated into the modelling process to acquire initial estimates for the system’s parameters for Quarter 3.2. Information from the KASOC website that accompanies the *Kepler* data, values generated using Kepler’s third law (assuming a circular orbit), and approximate estimates based on the aforementioned information were used as input parameters for JKTEBOP (see Table 4). From these approximate values JKTEBOP generated a fit to the data. The output parameters, listed in Table 4, were then incorporated into the modelling process using WD. All the values were directly transferable with the exception of the surface brightness ratio,  $e \cos \omega$  and  $e \sin \omega$ .

The WD code uses two separate parameters to define the light contributions of the two stellar components. Consequently, the surface brightness ratio generated by JKTEBOP was used as a guide when manually creating an initial synthetic model using WD. A value for the eccentricity was also generated by JKTEBOP, which required no initial estimate. From this value ( $e = 0.281$  with no formal errors given) the longitude of periastron was calculated to be  $\omega = 325.21^\circ$  using the value of  $e \sin \omega$ . The errors specified are the formal errors (Gaussian errors approximated by the WD code) and are not indicative of the true uncertainty in the values as they do not account for correlations between parameters.

As previously mentioned, JKTEBOP was initially incorporated into the modelling process to identify the orbital ephemeris of the system. However, whilst JKTEBOP’s rapid modelling technique was favourable for this task, the pronounced stellar distortion of KIC 4544587 goes beyond the limitations of this program. For this reason the WD code was used to further constrain the stellar parameters and

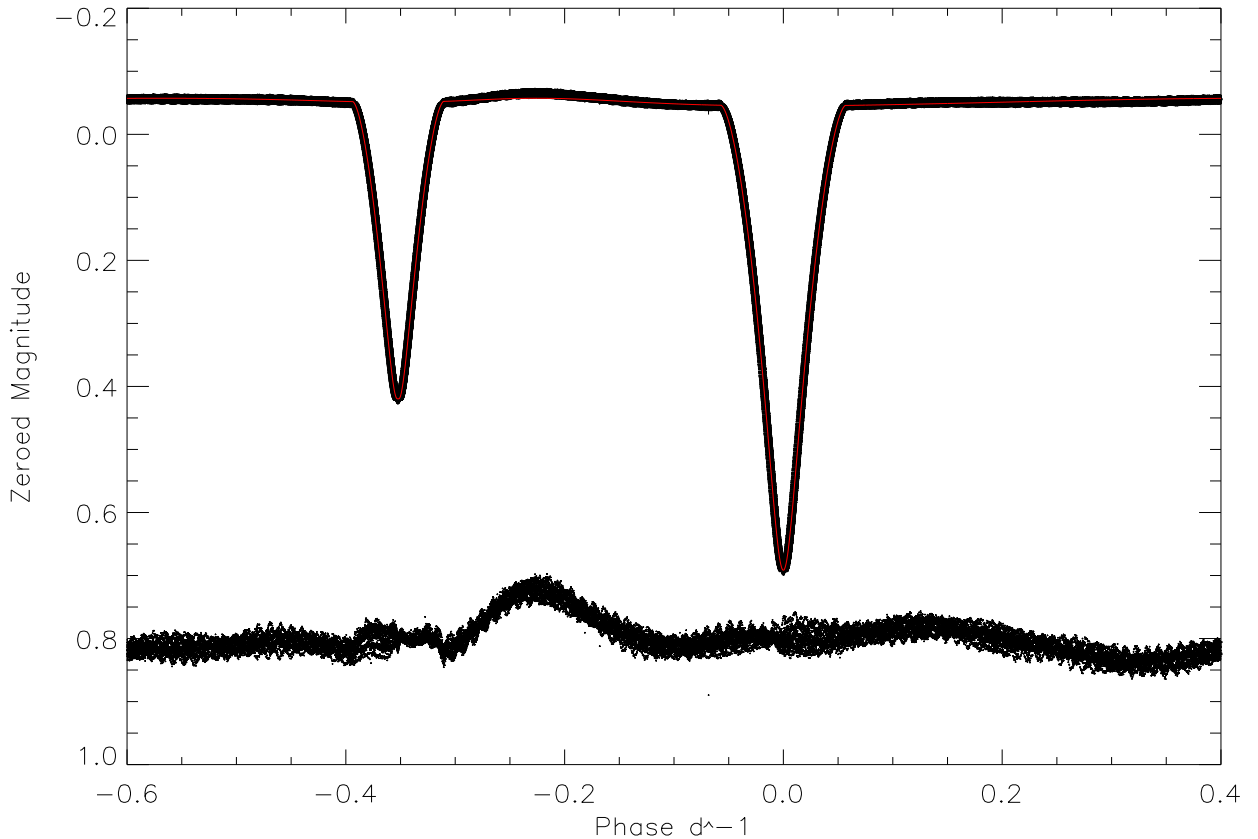


Figure 13: The phased data from Quarter 3.2 (black) and the model fit (red) from JKTEBOP. The residuals are displayed below the data, offset by 0.8 magnitudes and amplified by 10 for clarity.

arrive at a better fit.

### 4.3 Wilson and Devinney

The first version of the WD (Wilson & Devinney, 1971) code superseded previous binary modelling codes, such as the Russell model (Russell & Merrill, 1952), with a more direct treatment of reflection effects and an improved approach to gravity brightening. In 1976 Wilson & Sofia (1976) incorporated the ability to analyse radial velocities into the code. The code was further improved in 1979 to include binary eccentricity, non-synchronous rotation and the ability to fit light curves and radial velocities simultaneously (Wilson, 1979). The WD code uses a differential corrections algorithm to arrive at an optimal set of parameters that characterize the binary light curve.

The approach of the WD code is to combine the flux of discrete surface elements over the distorted stellar model, and to equate this to the observed flux. The number of surface elements on each stellar component is defined by two input parameters,  $N$  and  $NL$ , which signify the number of latitudinal and longitudinal divisions per hemisphere respectively (typical values range from 30–80 divisions per hemisphere but computational time increases linearly with the number of segments). An accurate account of the observed flux is obtained with the incorporation of effects such as limb darkening, gravity brightening, multiple reflection effects and the simple treatment of reflection using an inverse square law. In addition, horizon effects, which describe the treatment of the stellar boundary as seen by the

Table 4: The initial estimates used and subsequent values generated by JKTEBOP that were later incorporated in the modelling process using WD. The uncertainty specified is the one sigma uncertainty in the final digit as generated by JKTEBOP and is the formal error; hence it does not account for correlations between the parameters and is not indicative of the true uncertainty in the values.

Parameter	Initial Estimate	JKTEBOP	Uncertainty
Surface brightness ratio	0.7	0.7212	0.0024
Orbital inclination( $^{\circ}$ )	88	88.271	0.011
$e \cos \omega$	0.23	0.23114	0.00001
$e \sin \omega$	0.00	-0.16054	0.00032
Mass ratio	0.9	0.821	0.001
Orbital period (d)	2.18911	2.1891084	0.00000115
Epoch of primary minimum (BJD)	2455138.02	2455138.019814	0.000006

hypothetical observer, and eclipse effects, which describe how this boundary changes during eclipse, are considered in order to obtain the final parameter values for the stellar components.

#### 4.3.1 Binning the data

As the WD code is only able to compute up to 9000 data points at any given time, it was necessary to bin the data prior to input. Furthermore, binning the data significantly reduces the computational time required by the WD code to generate a fit to the data, which is extensive, especially for an eccentric system such as KIC 4544587. The binning program used was created by Southworth et al. (2004b) and is designed to phase bin the data into the user specified number of bins. For the short cadence data of Quarter 3.2 the light curve was folded using the previously identified period, and binned into 500 data points using a constant step of  $\Delta\phi = 0.002$ .

#### 4.3.2 Constraining the Model using WD

When modelling the data, the initial inputs were a combination of the information provided by KASOC (as a supplement to the *Kepler* data), values derived from this information and those generated by JKTEBOP (as discussed in §4.2.1 and listed in Table 4). As we do not yet have spectral data for this object, the temperatures of the stars are not tightly constrained. Consequently, the single temperature provided by KASOC (8255 K), which is a summation of the temperatures of the two stars (as a function of radius), was utilised as the starting value for the primary component in the modelling process. KASOC also provided a single  $\log g$  value ( $\log g = 4.0$ ), which was assumed for both components.

Prior to utilizing the differential corrections function of the WD program, an initial model was created. This was done by manually adjusting the stellar parameters to generate a synthetic model. Following this the values of the stellar light contributions, potentials, inclination and temperatures were adjusted to generate an approximately correct synthetic model that could be further constrained with the differential corrections minimiser. Once an initial model had been generated, the WD differential corrections algorithm was applied to the data in an iterative process. I further enhanced the minimising abilities of the WD code by utilizing a wrapper, JKTWD, created by Southworth et al. (2011), which generates automatic iterations and hence vastly reduces computational expense.

Table 5: Fixed parameters and coefficients for the WD best fit model to the *Kepler* light curve for Quarter 3.2. Here the primary and secondary stars are labeled as A and B respectively. The rotation is specified as a ratio of the stellar to orbital rotation and the numerical accuracy is defined to be the number of lateral (N) and longitudinal (NL) surface elements per hemisphere for each star.

Parameter	WD Specified Names	Values
Third light	EL3	0.0
log g (A)	Logg1	4.0
log g (B)	Logg2	4.0
Rotation (A)	Frot(A)	1.0
Rotation (B)	Frot(B)	1.0
Numerical accuracy (A)	N1	60
Numerical accuracy (B)	N2	40
Numerical accuracy (A)	N1L	30
Numerical accuracy (B)	N2L	20

#### 4.4 Multiple Iterations

When modelling a binary system with one or more pulsating components, multiple iterations are required. The method used involves subtracting the computed model from the original observed data, subsequent frequency analysis of the observed minus computed data (residuals), and finally, the removal of the pulsation frequencies from the original, detrended data. That which remains is a light curve predominantly free of pulsations for successive binary modelling. This enables the orbital characteristics to be modelled correctly without interference from the stellar pulsations. Furthermore, the Roche model assumes that any perturbations are negligible with respect to the instantaneous equipotential shape of the stellar components. On one hand the pulsations of KIC 4544587 are relatively small, although they still have a substantial affect on the light curve. Thus it was required that the pulsations were prewhitened so that an accurate model could be obtained. For each iteration care was taken to ensure that eclipse information was not excessively removed from the light curve. This was done by comparing eclipse depths before and after the subtraction of the pulsation frequencies.

Initially a mode was incorporated that places no constraints on the computation of the stellar parameters so that the pulsations could be fully separated from the light curve. For the final iteration the luminosities and temperatures of the stellar components were coupled so that the model obeyed Stefan-Boltzmann’s law. Three iterations were needed for modelling KIC 4544587, with further iterations having negligible effect determined by the values altering by less than their uncertainties. The fixed and free parameters, and their corresponding values for Quarter 3.2 can be found in Tables 5 and 6 respectively.

Fig. 14 demonstrates the theoretical model and residuals obtained for the third iteration. On one hand a direct comparison cannot be made because only one iteration was performed using JKTEBOP; however, compared to the model of Fig. 13, two points should be noted: primarily, in Fig. 14 the hump in the light curve that occurs after secondary minimum has been fitted to the extent that it is not visible in the residuals; and as the residuals are magnified by the same factor for Figs 13 and 14 (both have been multiplied by ten), it can be seen that the fit to the eclipses has improved greatly.

There is still a small amount of residual pulsation information remaining in the observed light curve

Table 6: Free parameters and coefficients for the best fit model to the *Kepler* light curve for Quarter 3.2. Here the primary and secondary stars are labeled as A and B respectively. The uncertainty specified is the one sigma uncertainty in the final digit, as generated by WD, and is the formal error; hence it does not account for the correlation between the parameters and is not indicative of the true uncertainty in the values.

Parameter	WD Specified Names	Values
Phase shift	PSHIFT	0.082646(1)
Semi-major axis ( $R_{\odot}$ )	A	11.00000(2)
Orbital eccentricity	ECCENTR	0.28375(5)
Longitude of periastron ( $^{\circ}$ )	OMEGA0	324.444(7)
Orbital inclination	INCLIN ( $^{\circ}$ )	88.24(7)
Mass ratio	MASSRAT	0.47714(6)
Primary mean temperature (K)	Teff(A)	8271(10)
Secondary mean temperature (K)	Teff(B)	6354(3)
Potential (A)	POT(A)	6.703(6)
Potential (B)	POT(B)	5.006(9)
Bolometric albedo (A)	ALB(A)	1.12(1)
Bolometric albedo (B)	ALB(B)	0.431(1)
Linear limb darkening coeff. (A)	LDU(A)	0.448(2)
Linear limb darkening coeff. (B)	LDU(B)	0.454(3)
Relative light contribution	HLUM	8.642(1)
Relative light contribution	CLUM	4.5468(1)
Gravity brightening (A)	GRAV(A)	1.064(1)
Gravity brightening (B)	GRAV(B)	0.480(1)

Table 7: The fractional radii of the stellar components derived from the best fit model for Quarter 3.2, as generated by the WD code.

Radius	Primary	Secondary
Pole	0.165180	0.141380
Point	0.167540	0.146400
Side	0.165730	0.142000
Back	0.167030	0.145250
WDLC mean	0.166029	0.142974

during eclipse phase which can be attributed to a slight discrepancy between the model and the light curve. There is also some residual pulsation during eclipse phase that occurs due to the change in relative light contributions as one star passes in front of the other. This either increases or decreases the observed amplitude of pulsation depending on the component that is being eclipsed. For this reason the pulsations are not fully removed during eclipse phase. Further discussion of the treatment of the residuals can be found in §5.

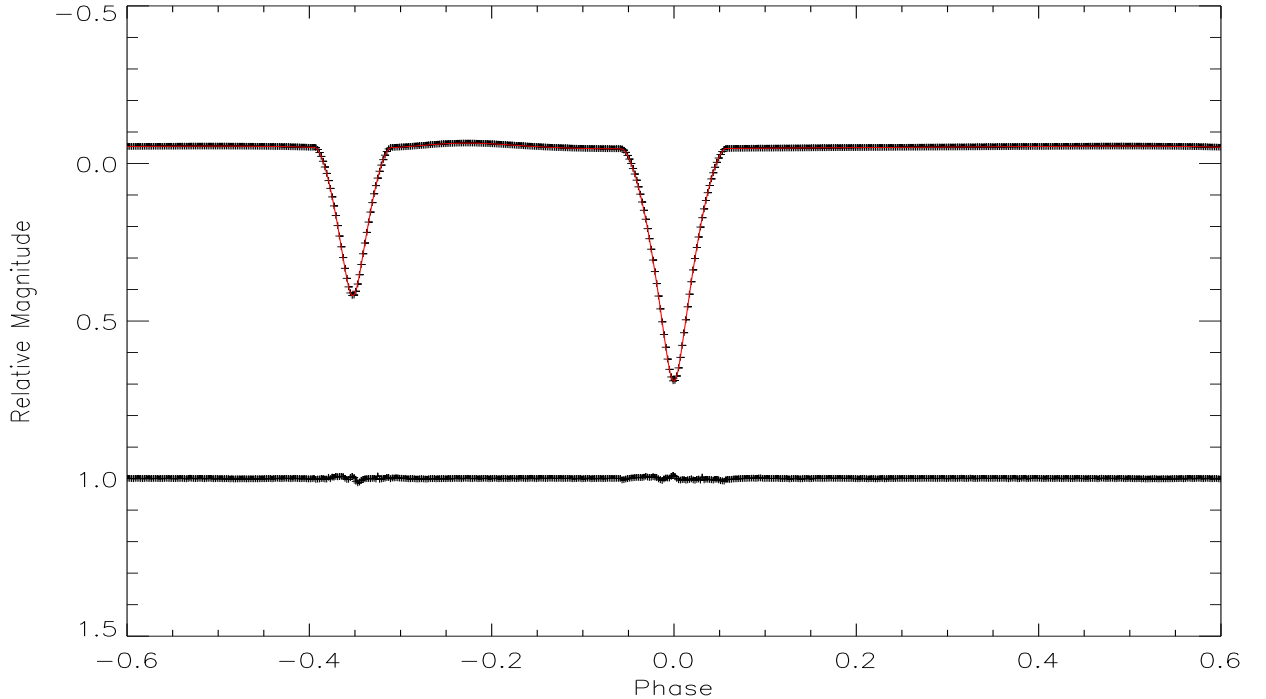


Figure 14: Observed light curve (black points) and theoretical model generated by the WD code (red line). The residuals (black dots), which are multiplied by ten, are offset from the light curves by 1.0 magnitudes for clarity.

The parameters generated by the WD code are indicative of a system with two oblate components in close proximity. The level of oblateness is demonstrated by the variation in fractional radii for the two stellar components shown in Table 7. The parameters obtained suggest that the primary component is within the  $\delta$  Scuti instability strip and the secondary a possible solar-like oscillator. We cannot, therefore, presume that only the primary component is pulsating. However, it is likely that only the pulsations of the primary have been detected due to the low amplitude of solar-like pulsations Kjeldsen & Bedding (2011). Neither component is a candidate for g mode pulsations independently. However, as in the case of KOI-54 (Welsh et al., 2011), tidal interactions have induced strong g mode pulsations. It is most likely that it is the primary component that is pulsating, although future spectroscopic investigation will provide a more definitive answer.

#### 4.4.1 Generation of Residuals

I wrote a piece of software that enabled the subtraction of the synthetic model from the original data. The objective of this was to enable the analysis of the stellar pulsations in the light curve, without influence from the binary features.

To achieve this the data were initially converted from the time domain to the phase domain. This

was done by subtracting the user specified zero point in time (in Truncated Barycentric Julian Date) from each data point, and dividing this value by the user specified period. The synthetic data were then interpolated so that the number of computed data points was equal to the number of observed data points for each phase. The synthetic model was then subtracted from the observed data, leaving only the residuals. The data were then converted back into the time domain.

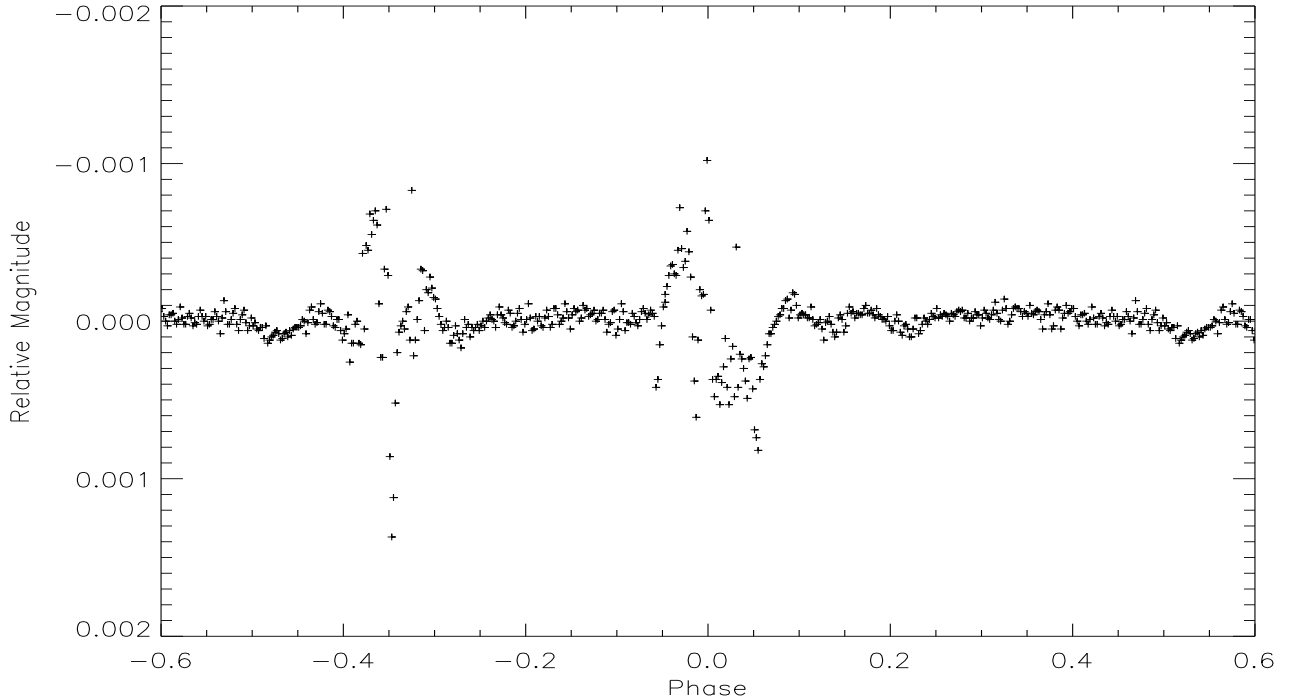


Figure 15: The residuals of the pulsation-free light curve after subtraction of the final, best-fit model for Quarter 3.2. A minimal amount of residual eclipse information remains in the phased data; for this reason the data points that lie within the eclipse phases were removed during pulsation analysis.

Subsequently, the instrumental trend was identified by fitting a low order polynomial to the residuals. The polynomial generated was then removed from both the residuals and the original data set. The polynomial selected for Quarter 3.2 was fifth order as, through the consideration of the detrended data, this appeared to generate an optimal fit to the instrumental trend.

Frequency analysis was then performed on the data to identify the pulsation periods, as specified in § 5. The identified modes were then prewhitened from the original data. This provided a light curve that was predominantly free of instrumental effects and pulsations, leaving only the binary characteristics. This allows for a more concise model of the binary system to be generated.

Once a new model had been created, this was again subtracted from the original, detrended data. Subsequently the process of determining the pulsation frequencies and amplitudes of the residuals was repeated. Three iterations were undertaken until the root mean square of the residuals, when the model was subtracted from the light curve with the pulsations removed, did not decrease with further iterations to three decimal places (the accuracy demonstrated by the WD code). The residuals generated through the subtraction of the final model from the pulsation-free light curve can be seen in Fig. 15. A comparison between the detrended, original light curve and the light curve with the pulsations removed was made after each iteration. This was to ensure that the pulsations were not being over-subtracted,

which would be highlighted by alterations in the depths of the eclipses.

## 4.5 PHOEBE

Despite the fact the Wilson-Devinney code has played a vital role in the determination of the binary characteristics of KIC 4544587 for Quarter 3.2, to model Quarter 7 including apsidal motion, PHOEBE (Prša & Zwitter, 2005) was incorporated into the modelling process. PHOEBE is based on the Wilson-Devinney code and provides an intuitive graphical user interface alongside many other improvements that make PHOEBE increasingly applicable to the high quality, precise *Kepler* data. These include: temperature determination through colour contrasting; uncertainty calculations through heuristical scanning algorithms (which scan parameter space by generating results from multiple starting points to determine the mean and standard deviation); the facility to phase-bin the data; updated filters for the various recent space missions including *Kepler*; and the ability to work with an unlimited number of data points.

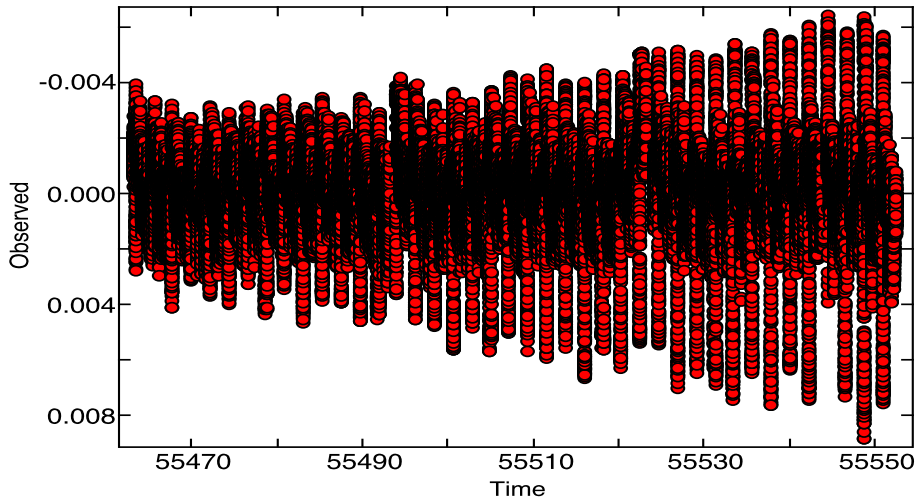


Figure 16: An image of the Quarter 7 residuals after subtraction of a model generated by PHOEBE. Here it can be seen that the large scale variations, which are due to the discrepancies between the model and the data, are increasing with time; although this could be due to an incorrect ephemeris, it is also indicative of apsidal motion. The y-axis is in relative flux units and the x-axis is Truncated Barycentric Julian Date.

When modelling Quarter 7, the deviation of the minima from a fixed ephemeris was apparent in the residuals; this is a signature of apsidal motion (see Fig. 16). It was also possible, however, that the ephemeris of the data had not been correctly identified. For this reason the presence of apsidal motion was confirmed through the identification of the anomalous period (see § 4.5.3). Following this the rate of apsidal advance was identified using PHOEBE. As apsidal motion occurs on relatively short time scales in KIC 4544587, to achieve a high quality model that is applicable to the complete data set, it was required that apsidal motion be incorporated into the model.

#### 4.5.1 Constraining the Model and Generation of Residuals using PHOEBE

As PHOEBE has an incorporated binning function, it was only required that the data be detrended prior to the modelling process. This was done using sigclip, which performs automated sigma clipping to determine a Legendre polynomial of user-specified order to fit the data. The method incorporated involved applying sigclip to the data using a threshold of 0.05 sigma below the light curve and 5 sigma above the light curve. This essentially eliminates the data points below the outer envelope of the light curve, enabling a fit to the outer envelope alone (Prša, A., private communication). Through the consideration, by eye, of orders 1–15, an 8<sup>th</sup> order Legendre polynomial was determined to be most suitable for the removal of all instrumental trends.

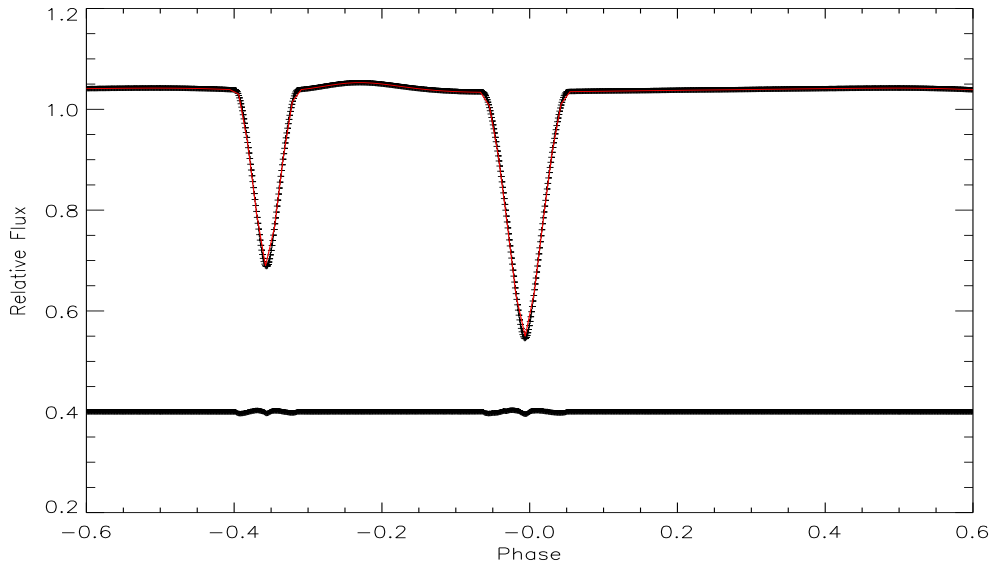


Figure 17: Theoretical (red line) and observed (black points) light curves, generated by the Wilson-Devinney code. The residuals (black dots), which are multiplied by ten, are offset from the light curves by 0.6 flux units for clarity.

Following this a synthetic model of the Quarter 7 data was generated by manually adjusting the initial input parameters, which were taken from the WD model for Quarter 3.2 (see Table 6). PHOEBE’s graphical user interface made this process efficient and allowed for a more intuitive adjustment approach. The method used when modelling the Quarter 7 data was to keep the luminosities and temperatures coupled for the whole modelling process; for this reason only the temperatures required manual adjustment as the luminosities were calculated as a function of temperature, normalised to the input light curve.

Once an approximate model had been created, the differential corrections algorithm was incorporated to improve the orbital fit to the data. As with the Quarter 3.2 data, it was required that the pulsations be prewhitened so that the orbital features could be tightly constrained. The values listed in Tables 8 and 9 are the fitted parameters and those generated after the second iteration using PHOEBE respectively. The values in Table 10 are the radii of the stellar components derived from the best fit model using PHOEBE (which can be seen in Fig. 17). As the *Kepler* data of Quarter 7 were released towards the later stages of this work, the complete analysis has not yet been undertaken and therefore must be considered as preliminary. However, although subsequent iterations may have slightly improved

Table 8: Fixed parameters and coefficients for the PHOEBE best fit model to the *Kepler* light curve for Quarter 7. The rotation is specified as a ratio of stellar to orbital rotation and the fine grid raster is the number of surface elements per quarter of the star at the equator and coarse grid raster is used to determine whether the stars are eclipsing at a given phase.

Parameter	Values
Third light	0.0
Primary rotation	1.0
Secondary rotation	1.0
Primary Bolometric albedo	1.0
Secondary Bolometric albedo	1.0
Primary gravity brightening	1.0
Secondary gravity brightening	1.0
Mass ratio	0.7
Primary fine grid raster	80
Secondary fine grid raster	80
Primary course grid raster	50
Secondary course grid raster	50

the values obtained for the orbital parameters, the increased number of iterations is far more important for the frequency analysis for two reasons: only low amplitude pulsations will remain in the data, which do not have a large effect on the binary modelling process; and as the data are phase binned prior to modelling, all residual pulsation (that is not commensurate with the orbital period) will essentially cancel. For this reason, however, the frequencies generated from the modelling of Quarter 7 are only considered preliminary until further iterations have been generated.

When modelling with PHOEBE the theoretical values for the albedo and gravity brightening exponents were held fixed. This was done to reduce the number of dimensions in phase space and thus generate a more realistic model. As the temperature of the secondary component, as determined by the WD code, is on the cusp between a radiative and convective envelope, the data were modelled with theoretical values for both occurrences and the results compared. Specifically, the data were modelled with the albedo and gravity brightening of the secondary component set to 0.5 and 0.32 respectively for the convective outer envelope and for the radiative envelope both the albedo and gravity brightening were set to 1.0. From the orbital fit it was determined that assuming a radiative envelope for both components gave the best outcome. In Fig. 18 a mesh plot of the system can be seen which shows the physical form of the parameters generated by PHOEBE.

#### 4.5.2 The Synchronicity Parameter

As it is evident from the study of Quarter 7 that the line of apsides is moving with time, and as the orbit is eccentric, it is also possible that the rotation of the stars is not pseudo-synchronous with the orbit. Pseudo-synchronicity is the closest an eccentric binary can get to a synchronous orbit, as in an eccentric orbit the components librate and so cannot be classed as fully synchronous. A quasi-synchronous orbit was thus investigated. The formula to identify the rate of stellar rotation with respect to the orbital rotation as specified by Hut (1981) is:

Table 9: Free parameters and coefficients for the best fit model to the *Kepler* light curve for Quarter 7. The uncertainty specified is the one sigma uncertainty in the final digit, as generated by PHOEBE, and is the formal error; hence it does not account for the correlation between the parameters and is not indicative of the true uncertainty in the values. The values for the limb darkening coefficients have been taken from the phoebe (2010) limb darkening tables and so do not have accompanying errors. Furthermore, error estimates are not given with the values for  $\log g$ , although these will be calculated upon the determination of the final parameters.

Parameter	Values
Phase shift	0.0766(1)
Semi-major axis (Rsun)	11.01044(2)
Orbital eccentricity	0.28315(9)
Argument of periastron (rad)	5.6892(5)
Orbital inclination <sup>o</sup>	87.82(1)
Primary mean temperature (K)	8172(1)
Secondary mean temperature (K)	7371(2)
Primary potential	6.928(4)
Secondary potential	6.576(4)
Orbital Period (d)	2.189116(1)
Apsidal Advance	0.0001178557(1)
Primary relative light contribution	8.824(6)
Secondary relative light contribution	4.227(3)
$\log g$ (Primary)	4.2333
$\log g$ (Secondary)	4.2268
Primary linear limb darkening coeff.	0.65367
Secondary linear limb darkening coeff.	0.66881
Primary non-linear limb darkening coeff.	0.28367
Secondary non-linear limb darkening coeff.	0.24226

Table 10: The fractional radii of the stellar components derived from the best fit model for Quarter 7, as generated by PHOEBE code.

Radius	Primary	Secondary
Pole	0.1692	0.1426
Point	0.1729	0.1460
Side	0.1699	0.1431
Back	0.1729	0.1460

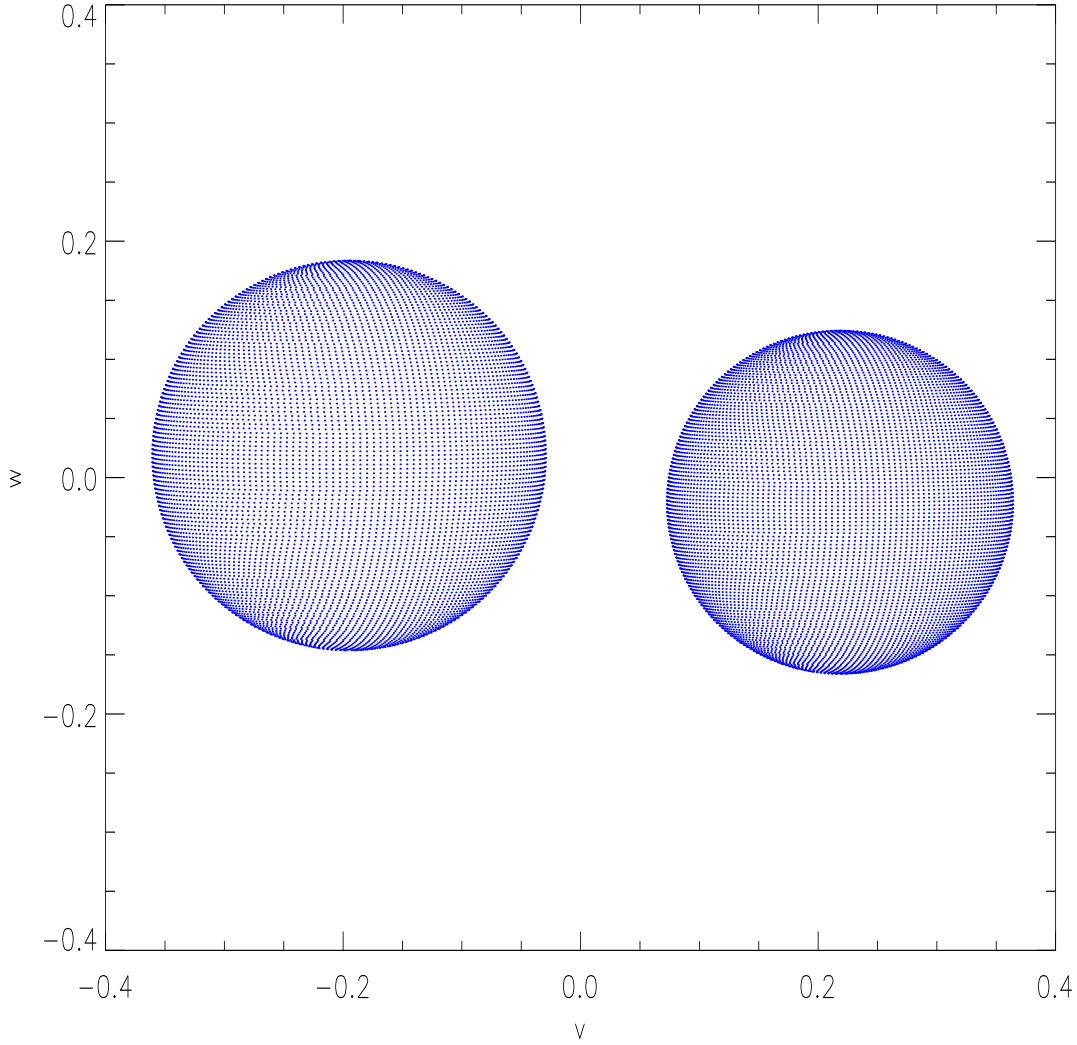


Figure 18: A mesh plot of the synthetic model of KIC 4544587 as generated by PHOEBE.

$$F = \sqrt{\frac{1+e}{(1-e)^3}} \quad (23)$$

where  $F$  is the ratio of stellar to orbital rotation and  $e$  is the eccentricity of the system ( $e = 0.28315(9)$ ). A quasi-synchronous orbit is an orbit where the rotation rate of the two components at periastron are assumed to be consistent throughout the orbit. The value for the quasi-synchronous rotation rate was found to be  $F = 1.87(1)$ , where the error is demonstrated by the value in the parenthesis and has been propagated from the formal error. This value was incorporated into the modelling process using PHOEBE. It can be seen in Fig. 19 that incorporating this value into the modelling process created a dip in the residual light curve after secondary minimum and did not generate an adequate fit. This suggests that if the components are rotating at a rate close to the quasi-synchronous value, that there would be a larger hump in the light curve after secondary minimum.

The orbital rotation rates were then fitted using PHOEBE with the already obtained model for Quarter 7 and the quasi-synchronous values calculated as initial estimates. It was found that the rotation

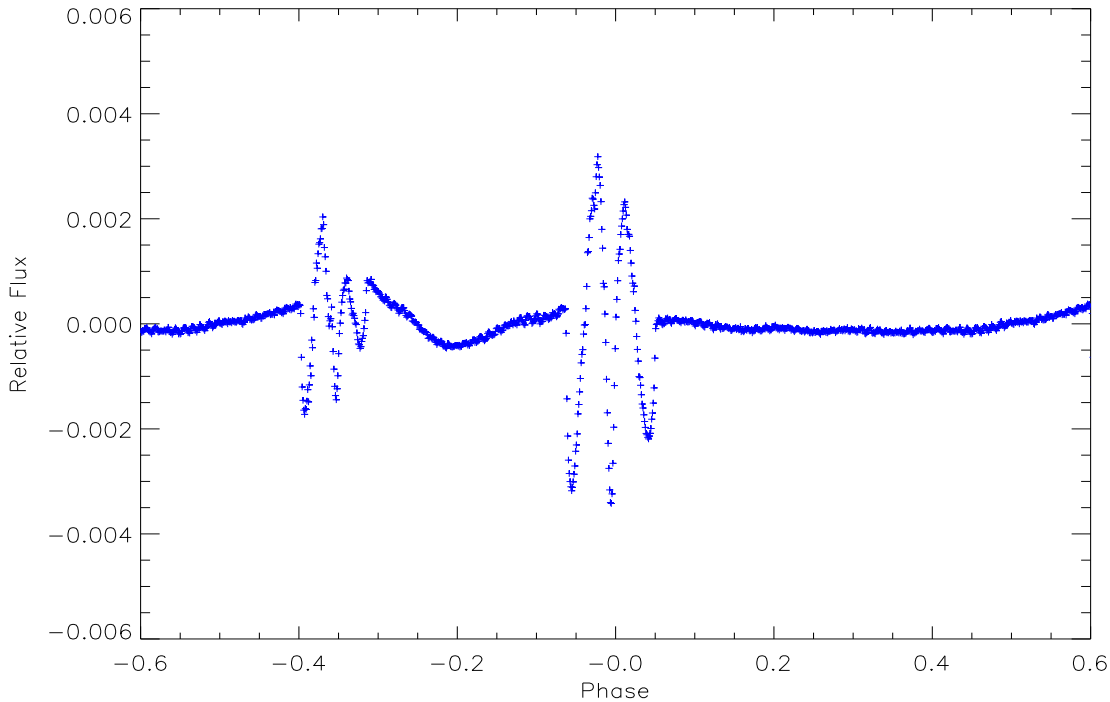


Figure 19: The residual data after subtraction of a model generated by PHOEBE with quasi-synchronous rotation incorporated. It can be seen that there is a dip in the residuals between secondary and primary eclipse, this has been generated by the incorporation of  $F = 1.87(1)$  as the value for pseudo-synchronous rotation. Furthermore, the fit generated to the eclipses is not ideal when incorporating this value (for reference, see Fig. 15 which depicts the residuals of the best fit model generated by WD for Quarter 3.2).

rates increased from the specified values using this method, but that the fit to the data did not improve. The starting values were then reduced to a value between quasi- and pseudo-synchronous (1.4) and finally fitted from a starting value of 1.0, which implies pseudo-synchronous rotation. For each iteration the synchronicity parameters for both stars increased with the application of the differential corrections method; however, the fit to the data appeared to deteriorate. As the best fit to the data was generated through assuming pseudo-synchronous rotation, it is likely that KIC 4544587 is approaching pseudo-synchronicity; for this reason the synchronicity parameters were reduced to 1.0, which was maintained for the remaining light curve modelling.

### 4.5.3 Apsidal Motion

Apsidal motion is the motion of the elliptical orbit about the centre of mass. As the orbit precesses, the line of apsides and hence longitude of periastron also advances with time. The longitude of periastron is a quantity that is measurable, and so its motion with time can also be measured; assuming that the motion is detectable over the duration of the data set. Furthermore, the motion of the line of apsides causes the phase of primary and secondary eclipse to move with respect to each other.

Following the initial indicators that the orbit of KIC 4544587 is undergoing apsidal motion, as seen in the residuals of Quarter 7 (see Fig. 16) and the difference in orbital periods obtained using PDM and ephemerides generated using JKTEBOP for Quarters 3.2 and 7, conclusive evidence of apsidal motion was sought. This was identified by phasing the total data set by a period which held the primary

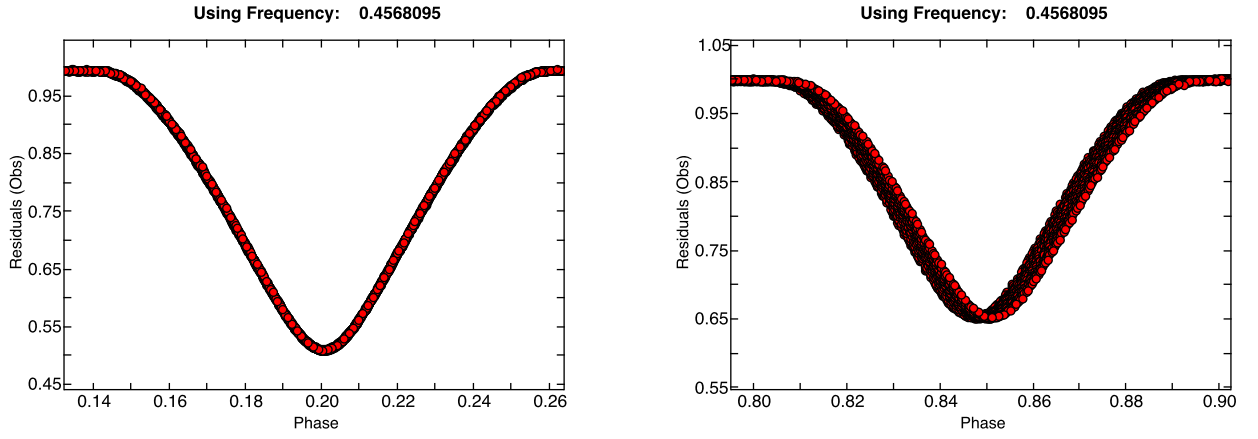


Figure 20: Two images of the total, LC data set, phased by a period of 2.189096 d and amplified to show *left panel*: the primary eclipse, and *right panel*: the secondary eclipse. The frequency selected represents the anomalous period of the data set. By selecting the anomalous period the primary eclipse remains fixed at the same phase whereas the secondary eclipse becomes smeared due to the motion of the line of apsides. The y-axis is measured in relative flux units.

eclipse in a fixed position, but generated a smearing effect with the secondary eclipse, as seen in Fig. 20. This period is known as the anomalous period and is the time elapsed from primary eclipse to primary eclipse. Thus it does not account for the motion of the eclipses within the orbit due to the motion of the line of apsides. Consequently, the anomalous period is not the sidereal period of the orbit. The anomalous period was identified, by eye, as 2.189096 d. This was done by adjusting the orbital frequency to arrive at the lightcurve in Fig. 20 where one eclipse is well defined in phase space and the other is smeared. Despite the fact the determination is not precise, the identification of an anomalous period demonstrates that the system is undergoing apsidal advance.

Subsequently, to determine an initial estimate of the advance of periastron a section of data containing a complete orbit was removed from the beginning of the data set and the end of the data set. These data were then modelled individually by maintaining the previously determined parameters, but allowing the longitude of periastron and phase shift to be fitted. Once a fit had been obtained, the value of the longitude of periastron was recorded. For the first orbit in the data set, where primary minimum occurs at  $\text{BJD} = 2454954.1469(5)$ , the periastron longitude was determined to be  $5.6601(2)$  rad. For the final orbit, where primary minimum occurs at  $\text{BJD} = 2455551.7513(2)$ , the longitude of periastron was identified as  $5.7052(2)$  rad. This generated an approximate value for the advance of periastron of  $d\omega/dt = (7.546 \pm 0.0005) \times 10^{-5} \text{ rad d}^{-1}$ .

This value was subsequently incorporated into the modelling of the complete data set, where the data from Quarters 3.2 and 7 were converted into LC. Initially, to constrain the estimate further, segments of data that were approximately twenty orbits apart were modelled. This was done by adjusting the rate of apsidal advance (with slight adjustments to the period once the fit was almost constrained). The luminosity was also fitted as this parameter requires recalculation every time a new data set is added. The period was adjusted so that the true period could be identified as opposed to the anomalous period. *The rate of apsidal advance was found to be  $0.0001179(1) \text{ rad d}^{-1}$ , which gives  $145.9(1) \text{ yr}$  for one complete precession.*

## 4.6 Comparison of Quarter 3.2 and Quarter 7 Results

When modelling the Quarter 3.2 data, prior to the final fit, the WD code was applied in such a way that the binary system was modelled without constraining the relation between luminosity and temperature. Whilst the temperatures can be calculated later, other parameters that are a function of temperature, such as gravity brightening and limb darkening, are not consistently defined. We incorporated this method primarily as the inherent pulsations in KIC 4544587 posed an issue when generating an initial fit to the data. Conversely, when using PHOEBE we imposed the constraint between the temperatures and luminosities constantly throughout the fitting process in order to yield a more consistent treatment of temperature dependent values.

There are contradictory beliefs as to whether it is acceptable to approach modelling using this technique. As the pulsations of KIC 4544587 are affecting the shape of the light curve, it is unrealistic to assume that an accurate binary model can initially be achieved. For this reason it can be argued that it is advantageous to fit a model that generates the smallest residuals in the initial modelling stages. This enables the majority of the frequency information to be removed, thus allowing further modelling with a mode that incorporates the Stefan-Boltzmann law through the application of Kurucz model atmospheres (in the case of detached systems for WD; mode 2).

It is also arguable, however, that subtracting an initial unphysical model will inject anomalous information into the data and hence end in a fit that is inaccurate. The alternative is therefore to generate an initial fit that follows the Stefan-Boltzmann law, although this may also be an incorrect fit as it is still fitting the pulsations inherent in the system. For this reason the initial binary fit generated for Quarter 3.2 was done with the former method and the second binary fit generated for Quarter 7 was done with the latter method and the results compared.

Due to the rotation of the *Kepler* CCD, the two data sets of Quarter 3.2 and Quarter 7 have been taken using the same CCD pixels, which is advantageous as it will reduce any discrepancies caused by instrumental effects. Furthermore, as PHOEBE is based on WD, a comparison of the results can be made with only minimal considerations to the modelling programs themselves (with the largest difference being the implementation of the *Kepler* photometric pass band). There are, however, several differences in the methods used that inhibit a direct comparison of the two sets of data, all of which are discussed below.

When modelling the data without the temperatures coupled, using WD, it was found that the initial orbital fit was more tightly constrained. This was determined by the smaller discrepancy between the model and observations, during eclipse phase, for WD ( $\pm 0.003$  relative magnitudes) than for PHOEBE ( $\pm 0.005$  relative flux units). However, this can be partially attributed to the use of relative flux with PHOEBE and relative magnitudes for WD, although in relation to the inherent pulsations, there was less residual eclipse information in the WD generated residuals. Furthermore, this discrepancy could also have occurred as a direct consequence of maintaining the Stefan-Boltzmann law throughout the fitting process with PHOEBE and not with WD. Hence, although the fit generated with PHOEBE was not as well constrained, it is possible that it is a more realistic fit to the data. The true temperatures of the components will be determined with the acquisition of spectroscopic data, and consequently the preferable method will be identified.

Other differences between the analysis of the two data sets are: the albedos and limb darkening

exponents were fitted with WD but not with PHOEBE; the data were converted into magnitudes for use with WD but not with PHOEBE; the data sets are different lengths; and apsidal motion was incorporated into the modelling process with PHOEBE. Furthermore, different pass bands were utilised for the two quarters, for Quarter 7 the *Kepler* mean pass band was used with PHOEBE, whereas for Quarter 3.2, using WD, the Cousins R band was used (as the *Kepler* pass band was not available). It is expected that from this difference alone a  $\sim 10\%$  discrepancy will occur in the results.

An obvious difference between the results of the two methods is that the WD program, through the fitting of the temperatures, albedos and gravity brightening exponents, generated values that are suggestive of a secondary with a convective outer envelope. Whereas, when modelling with PHOEBE, the albedos and gravity brightening exponent were not fitted; rather the theoretical values for both a radiative and convective outer envelope were applied to the secondary component and the fits compared. Using this method it was found that the best fit to the data was achieved when assuming that the secondary component has a radiative outer envelope (or that the convective envelope is negligible).

Furthermore, the temperatures of the two stellar components were both fitted in each of the modelling attempts (although only one temperature was fitted at a time to avoid correlation issues). While the temperature of the primary star only differs by 100 K for the two data sets, the temperature of the secondary differs by 1000 K. It is expected that this discrepancy is the cause of the variation in the albedos and gravity brightening exponents, especially since the temperature determined by WD (6354 K) is on the cusp between a radiative and convective envelope, as defined by Claret (2001). The spectroscopic temperatures of the two components are not currently available, however, it will be very interesting to ascertain which of these results is closer to the observed quantities.

The gravity brightening exponents generated using WD were 1.064(1) and 0.480(1) and the values for the albedo were 1.12(1) and 0.431(1) for the primary and secondary stars respectively, where the values in the parenthesis demonstrate the formal error in the last digit. Primarily it can be seen that both values for the primary component are greater than 1.0 (the theoretical value adopted for the gravity brightening exponents and albedos of the primary and secondary when using PHOEBE) and thus are unphysical when considering the formal errors. However, the formal errors are a gross underestimation of the errors involved as the correlations between parameters and uncertainty related to the input parameters (such as temperature) are not considered. For the secondary component the value generated for the albedo is smaller than the theoretical value for convective envelopes (0.5) and much smaller than the theoretical value for radiative envelopes (1.0). The value for the gravity brightening exponent of the secondary is in between the theoretical value for a convective (0.32) and radiative (1.0) outer envelope and thus is the most realistic value generated of these parameters. Although the values generated for the albedos and gravity brightening exponents are not all physical and differ from those obtained using PHOEBE, it was found that the orbital fit substantially improved when allowing these parameters to be fitted. This was also found by Southworth et al. (2011) when using WD to model *Kepler* data (KIC 10661783); although the albedo of the primary component was found to be  $2.69 \pm 0.012$  which is significantly larger and more unrealistic than that found here. The significance of this is that there appears to be a consistent discrepancy, as suggested by Claret (2001), between the theoretical values for the albedos and the highly precise *Kepler* observations.

The values generated by WD for the luminosities of the primary and secondary components are 8.642(2) and 4.35468(1) respectively, and those generated by PHOEBE are 8.824(6) and 4.227(3) (all in

arbitrary units normalised to the light curve). Consequently, for WD, the ratio of the light contributions is 1.90067(4), whereas for PHOEBE the ratio is 2.0879(7). The difference between the two ratios is large, especially when considering that the luminosity ratio is well defined in the light curve. This suggests that the different approaches have had a large impact on the luminosities and thus temperatures during the modelling processes, although these differences could also have arisen from the use of different programs (where a 10% discrepancy can be attributed to the different pass bands alone), data or because a local minimum has been located instead of the global minimum.

When fitting the data using WD, the linear limb darkening method was incorporated. However, with PHOEBE, the logarithmic law was adopted. It was found that the fit was not ideal when incorporating either of these laws, as remnant eclipse information still remained in the shoulders of the minima irrespective of the law incorporated. The linear law was incorporated when using WD as it appeared to give the best fit. The logarithmic law was incorporated for use with PHOEBE as this is theoretically the most applicable law for use in systems with  $T_{\text{eff}} < 9000 \text{ K}$  (Prša & Zwitter, 2005). It appears that, due to the precise nature of the *Kepler* data, the assumption that the limb darkening can be defined by these laws is no longer applicable.

The  $\log g$  value provided by KASOC for KIC 4544587 was  $\log g = 4.0$ . This single estimate was held fixed for both components when modelling with WD. However, when using PHOEBE the values for  $\log g$  are estimated by phoebe as a function of stellar temperature and potential for each individual component. The values determined by PHOEBE were  $\log g = 4.23$  for the primary and secondary components (where no formal errors are given). The difference in values between those obtained by WD and PHOEBE are likely to have affected the outcome of the modelling process. However, when considering the fractional radii of the stellar components, the secondary component has approximately the same values for the two data sets, whereas, the fractional radius of the primary is larger in the model generated by PHOEBE (see Tables 7 and 10). As both components have the same values for  $\log g$ , within their respective models, it appears that the variation in  $\log g$  values did not have a large effect on the values of the radii and subsequently the models themselves.

When using PHOEBE, due to the obvious apsidal motion present in Quarter 7 alone, the rate of apsidal advance was also fitted in the modelling process. This was performed after a model fit had been generated to the binned data of Quarter 7. The incorporation of apsidal advance into the model only had an effect on the phase shift, which decreased from 0.0774(2) to 0.0766(1), and the period, which increased from 2.189112(2) to 2.189116(1). Therefore the determination of apsidal motion did not influence the outcome of the remaining model parameters and thus did not contribute to any other discrepancies.

## 5 Frequency analysis

As a pulsating star expands and contracts, the sound waves that pass through it carry vital information about the stellar interior. These sound waves penetrate to different depths and provide information about the temperature, density and chemical composition of the cavity in which they are contained. Through the analysis of these modes, information pertaining to the stellar interior such as structure, rotation and transitional regions can be determined through asteroseismic modelling. Furthermore, by looking for frequency patterns and spacings, information about tidal interactions can be inferred.

### 5.1 Identification of Pulsation Frequencies

Two programs were used for the identification of frequencies in the light curve residuals of KIC 4544587. These were PERIOD04 (Lenz & Breger, 2004) and a Fourier transform program used in conjunction with a least squares program, both created by Kurtz (1985). The former of the two has a graphical user interface and allows for the frequency range and time step to be specified and subsequently performs a least squares fit to determine the amplitudes and phases of all the identified frequencies simultaneously. The latter of the two programs has the advantage of allowing for the removal of the determined frequencies from any data set, not just that from which they were determined. This enables the removal of the frequencies, which were generated from the residuals, from the original, detrended light curve. Tests have confirmed that both programs generate the same results and so the use of two programs is due to their ease of use for the various applications.

Following the first iteration the frequencies in the residual data were identified. To avoid the identification of frequencies that were remnants of the orbital fitting process, the data were masked prior to analysis. This was done by generating a computer program that converts the data from the time domain into the phase domain and removes data points at specified phase ranges. The phase ranges selected for the removal of data points were: 0.942–0.057 and 0.605–0.690. These ranges were identified by eye and denote primary and secondary minima respectively. Once the data during eclipse phase had been removed the remaining data were converted back into Truncated Barycentric Julian Date. The frequencies identified for the final iteration of Quarter 3.2 can be seen in Table 11.

One of the difficulties that arose was the determination of the noise level. It was decided that, although there were many frequencies remaining, only frequencies greater than  $20 \mu\text{mag}$  (twice the  $\sim 10 \mu\text{mag}$  noise level) would be removed. When identifying the peaks using the Period04, it was apparent that two peaks were not resolved. This was demonstrated by the increased uncertainty in the amplitude with respect to the standard amplitude error of the data set (the uncertainty in the amplitude is not related to the phase, frequency, or amplitude of the individual peak, but rather is a function of the noise level). Unresolved peaks can be problematic when performing a least squares fit as it is possible that the amplitudes of unresolved frequencies will increase dramatically in an attempt to account for the discrepancy in the resolution. This did not occur with the two unresolved peaks identified as the amplitudes remained approximately the same (for a discrepancy the expected increase would be orders of magnitude) and so they were prewhitened from the data set.

Further issues were encountered when fifteen harmonics of the orbital frequency were identified in the residuals (highlighted in red in Table 11), as this can be a sign of a bad orbital fit to the data. If a bad fit is generated, the imprint it leaves on the residual data will repeat each orbital phase. Consequently,

Table 11: The identified pulsation frequencies and their corresponding amplitudes and phases for Quarter 3.2. The values highlighted in red are orbital harmonics to an accuracy of  $3\sigma$  or greater. The values in parenthesis give the  $1\sigma$  uncertainty in the previous digit. The uncertainty in the amplitude is 0.0017 mmag.

Designation	Frequency ( $\text{d}^{-1}$ )	Amplitude (mmag)	Phase
$\nu_1 = 3\nu_{orb}$	1.37009(8)	0.772	0.5169(7)
$f_2$	2.01268(5)	0.576	0.8696(5)
$\nu_3 = \nu_{orb}$	0.45614(5)	0.523	0.7221(5)
$f_4$	3.4689(2)	0.386	0.892(2)
$\nu_5 = 4\nu_{orb}$	1.8279(1)	0.370	0.757(9)
$\nu_6 = 2\nu_{orb}$	0.9139(2)	0.351	0.988(2)
$\nu_7 = 7\nu_{orb}$	3.1975(8)	0.310	0.529(7)
$\nu_8$	48.0174(1)	0.285	0.9868(9)
$\nu_9$	41.3701(1)	0.253	0.652(1)
$\nu_{10} = 97\nu_{orb}$	44.3067(2)	0.201	0.985(1)
$\nu_{11}$	44.8477(2)	0.195	0.395(1)
$\nu_{12} = 5\nu_{orb}$	2.2824(8)	0.161	0.6770(7)
$\nu_{13}$	46.1929(2)	0.153	0.815(2)
$\nu_{14}$	1.6015(6)	0.130	0.850(5)
$\nu_{15}$	39.5423(3)	0.118	0.985(2)
$\nu_{16}$	44.8178(3)	0.111	0.953(2)
$\nu_{17}$	46.5791(4)	0.085	0.917(3)
$\nu_{18}$	38.2272(4)	0.079	0.549(3)
$\nu_{19}$	43.4460(4)	0.079	0.981(3)
$\nu_{20} = 98\nu_{orb}$	44.7595(5)	0.065	0.959(4)
$\nu_{21} = 8\nu_{orb}$	3.6537(8)	0.063	0.569(7)
$\nu_{22}$	47.9358(3)	0.052	0.509(3)
$\nu_{23}$	48.0590(7)	0.050	0.611(6)
$\nu_{24}$	47.9408(4)	0.049	0.739(4)
$\nu_{25} = 10\nu_{orb}$	4.5746(9)	0.046	0.979(8)
$\nu_{26}$	40.0533(6)	0.045	0.492(5)
$\nu_{27} = 97\nu_{orb}$	44.3600(10)	0.045	0.904(9)
$\nu_{28} = 95\nu_{orb}$	43.3928(10)	0.042	0.589(9)
$\nu_{29} = 105\nu_{orb}$	47.9825(1)	0.042	0.127(1)
$\nu_{30}$	5.4802(7)	0.041	0.181(6)
$\nu_{31}$	44.9360(10)	0.041	0.735(9)
$\nu_{32}$	1.6315(7)	0.040	0.468(6)
$\nu_{33}$	46.75720(6)	0.040	0.4760(5)
$\nu_{34}$	47.11179(7)	0.038	0.9925(6)
$\nu_{35}$	1.5748(11)	0.038	0.667(9)
$\nu_{36}$	46.6740(8)	0.038	0.268(7)
$\nu_{37}$	47.5896(1)	0.035	0.819(1)
$\nu_{38}$	5.0240(8)	0.033	0.515(7)
$\nu_{39}$	41.4234(3)	0.033	0.136(3)
$\nu_{40}$	39.9785(3)	0.032	0.128(3)
$\nu_{41} = 101\nu_{orb}$	46.1229(9)	0.032	0.326(8)
$\nu_{42}$	42.9999(3)	0.032	0.201(3)
$\nu_{43}$	43.26790(9)	0.031	0.8796(8)
$\nu_{44}$	43.4826(5)	0.031	0.136(4)
$\nu_{45}$	0.1065(8)	0.030	0.108(7)
$\nu_{46}$	0.1731(8)	0.029	0.316(7)
$\nu_{47} = 9\nu_{orb}$	4.1118(10)	0.025	0.407(9)
$\nu_{48}$	0.6576(9)	0.024	0.067(9)
$\nu_{49}$	3.0114(8)	0.020	0.689(7)

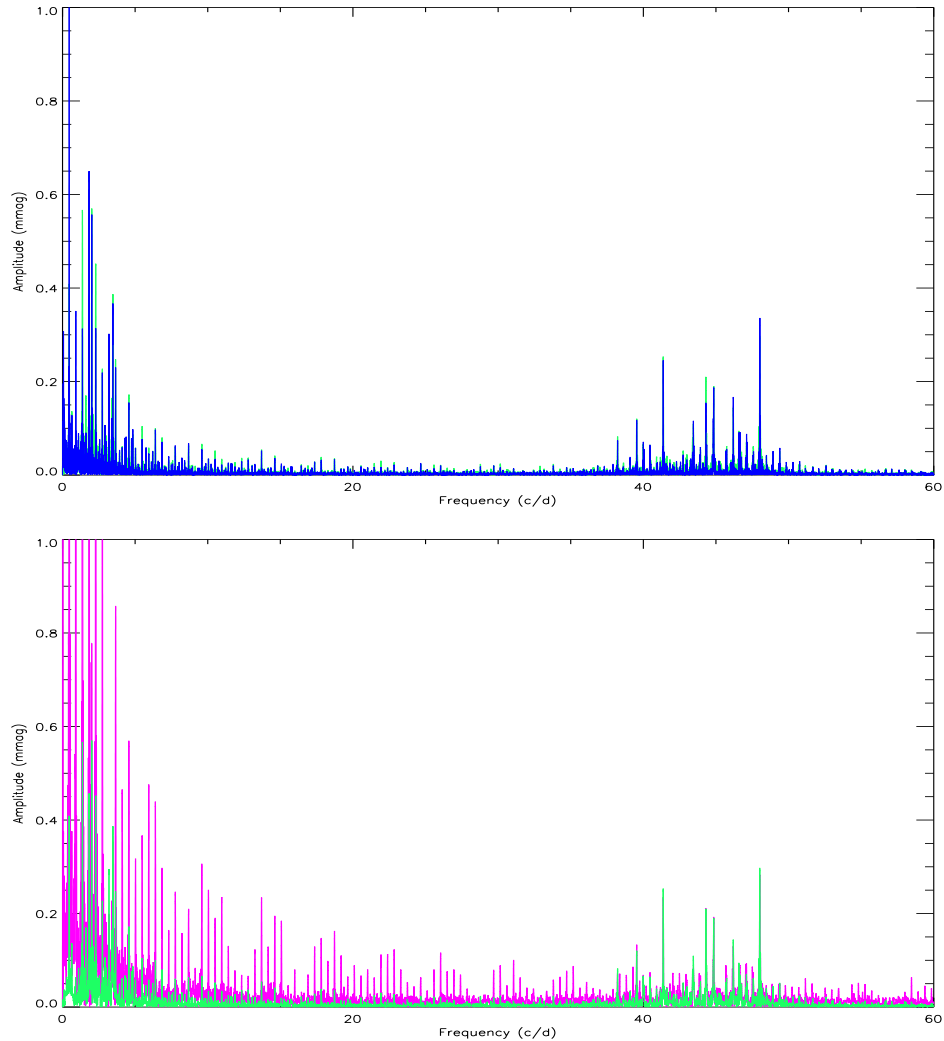


Figure 21: *Top panel:* A Fourier transform of the masked Quarter 3.2 residual data (green) and the masked Quarter 7 residual data (blue). The Quarter 7 data have been converted into relative magnitudes to ensure a fair comparison. *Bottom panel:* A Fourier transform of the masked Quarter 3.2 residual data (green) and the Quarter 3.2 original data with the eclipses masked (pink). The amplitude has been extended only to 1.0 mmag so that the details can be seen in the relevant areas.

a significant peak that is a multiple of the orbital frequency will occur in the Fourier transform due to the remnant orbital information. Initially only the frequencies that were not orbital harmonics were removed from the light curve. This light curve was subsequently modelled to further improve the orbital fit. However, this left visible oscillations in the data. For this reason all frequencies including harmonics were removed from the data. Further discussion on the implications of this can be found in §5.2

On the final iteration the frequencies were analysed extensively by assessing each one individually. As the residuals were masked to remove any residual modelling effects each true frequency had an increased amount of window pattern than would otherwise have been present. Consequently, the likeliness of cross talk between the frequencies was increased. For this reason care was taken in extracting the frequencies as the false identification of modes could generate an unrealistic asteroseismic stellar model. The frequencies were subtracted individually and for each frequency the effect on the Fourier transform was considered. The removal of each frequency did not affect the amplitude of the remaining or previously identified peaks in a significant way.

The top panel of Fig. 21 displays the Fourier transforms for the masked data of Quarter 3.2 and the masked data of Quarter 7, converted into relative magnitudes. The two Fourier transforms were generated independently from two different data sets, and modelled using slightly different approaches. However, it can be seen that the prominent peaks for both data sets lie at the same frequencies. This can further be seen through the comparison of the wavelet analysis graphs in §5.3. Furthermore, it is worth noting that the frequency analysis performed on Quarter 7 is only in the preliminary stages as only the initial model has been subtracted from the data. The reason for this is that the *Kepler* data is distributed on a quarterly basis and the Quarter 7 data was only recently acquired.

In the bottom panel of Fig. 21 a Fourier transform of the Quarter 3.2 data is displayed for both the masked residual data, and the unmodelled data with the eclipses masked. Primarily, this demonstrates the amount of orbital information that has been removed from the light curve through modelling. It is also evident that the p modes present in the light curve are not present due to a bad orbital fit. The amplitude range has only been extended only to 1.0 mmag since, although the amplitudes of the unmodelled data extend to amplitudes greater than 2.5 mmag, the relevant detail is more visible on this scale.

### 5.1.1 Period-Density Relation

There is a strong relation between the period of a mode and the mean density of a star:

$$Q = P \sqrt{\frac{\rho}{\rho_{\odot}}} \quad (24)$$

where  $Q$  is the pulsation constant,  $P$  is the period and  $\rho$  is the density. Through this relation an empirical formula has been generated that enables the identification of the pulsation constant through the determination of a star's period, surface gravity,  $g$ , Bolometric magnitude,  $M_{\text{bol}}$ , and effective temperature,  $T_{\text{eff}}$ :

$$\log Q = -\log f + 0.5 \log g + 0.1 M_{\text{bol}} + \log T_{\text{eff}} - 6.456 \quad (25)$$

Through the knowledge of the pulsation constant, the radial overtone of a mode can be inferred. The fundamental radial mode of a  $\delta$  Scuti star has a pulsation constant value of  $Q = 0.033$  and a first overtone value of  $Q = 0.025$  (Breger, 2000). Conversely, the expected period of a mode can also be identified through the knowledge of the pulsation constant specific to that mode and the aforementioned stellar values.

For KIC 4544587, eq. 25 was implemented using  $\log g = 4.0$ ,  $M_{\text{bol}} = 2.5$ ,  $T_{\text{eff}} = 8271$  K and  $Q = 0.033$  from which the fundamental radial mode was calculated to be at  $\nu = 13.9 \pm 2.5$  d<sup>-1</sup>. There do not appear to be any prominent modes at this value in the frequency spectrum. This suggests that the p modes in the data are high overtone p modes. The uncertainties are estimated at 18% of the  $Q$  value, as demonstrated by Breger (1990), and are a consequence of the approximated uncertainty in the observed quantities.

## 5.2 Indications of Tidal Interactions

An indicator of tidal interactions in binaries is a frequency or set of frequencies that are exact multiples of the orbital frequency (orbital harmonics). Such pulsation frequencies signify that the gravitational forces, generated by the tidal interactions of the binary system, have resonated with one of the natural eigenfrequencies present in the star. In an eccentric binary system, the gravitational forces acting on the components are time dependent due to the change in orbital separation; however, due to the dynamics of binary systems, they are dependent on orbital phase (Moreno et al., 2011). This suggests that if the orbital frequency, or integer multiple of the orbital frequency, is close enough to a natural mode of a binary star, and the gravitational interaction between the binary components is strong enough; it is possible for resonant modes to be excited.

During periastron passage the components of KIC 4544587, according to the models generated, have a surface-to-surface separation of  $5 R_{\odot}$  ( $\sim 8 R_{\odot}$  from centre-to-centre). Furthermore, the eccentricity of the system is  $e = 0.28375 \pm 0.000005$  (where the value is taken from the Quarter 3.2 model and the error is the formal error). The combination of these two aspects of KIC 4544587, alongside the  $\delta$  Scuti nature of the primary component, make KIC 4544587 a good candidate for tidal resonance.

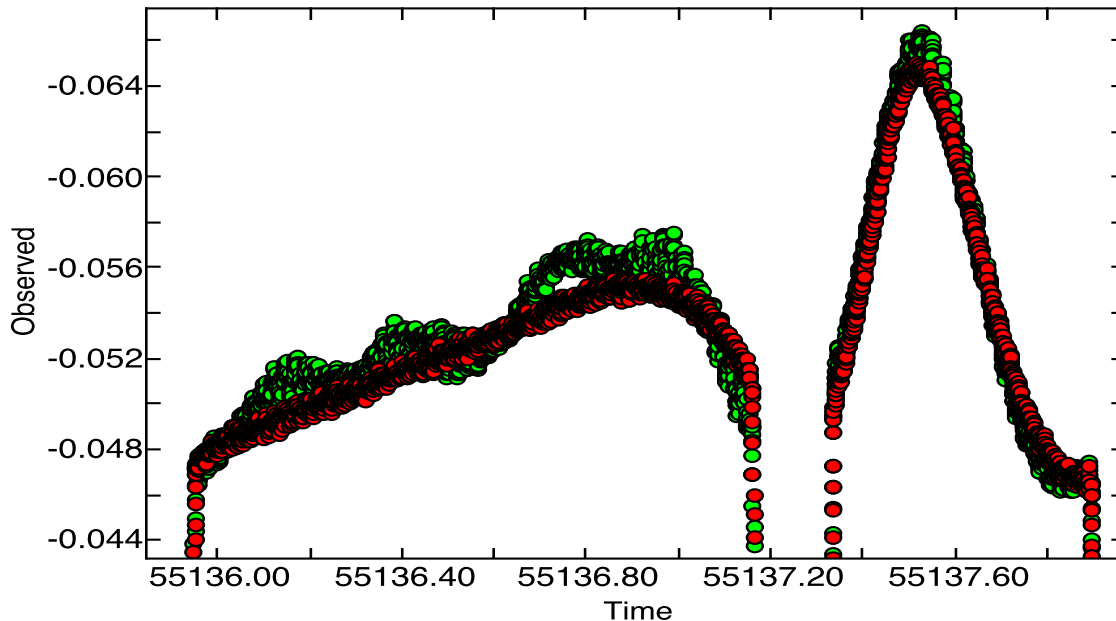


Figure 22: A comparison between the Quarter 3.2 data with all the frequencies removed (red), and with all the frequencies except the orbital harmonics removed (green). The residual features in the green light curve appear to be pulsations, suggesting that the harmonic frequencies are indeed intrinsic to KIC 4544587, and not generated through an inadequate orbital fit. The y-axis is measured in relative magnitudes and the x-axis is measured in Truncated Barycentric Julian Date (BJD - 2 400 000).

When analysing the residuals of KIC 4544587, from Quarters 3.2, 15 frequencies that are multiples of the orbital frequency were identified: nine g modes and six p modes. The data were masked to reduce the possibility that this was caused by modelling issues, as specified in § 5.1. This marginally decreased the amplitudes of the frequencies that are multiples of the orbital frequency, however, they still remained prominent and well above the noise threshold. In Fig. 22, an enlarged image of one orbit

within the Quarter 3.2 data can be seen with all the frequencies down to  $20 \mu\text{mag}$  removed (red) and with only the frequencies that are not orbital harmonics removed down to the same threshold (green).

As the signature of tidally excited modes is one or more frequencies that are multiples of the orbital frequency, the apparent residual pulsation remaining in the green light curve is highly indicative of tidal resonance. Future spectroscopic observations will allow the orbital fit to be more tightly constrained and thus further strengthen this argument.

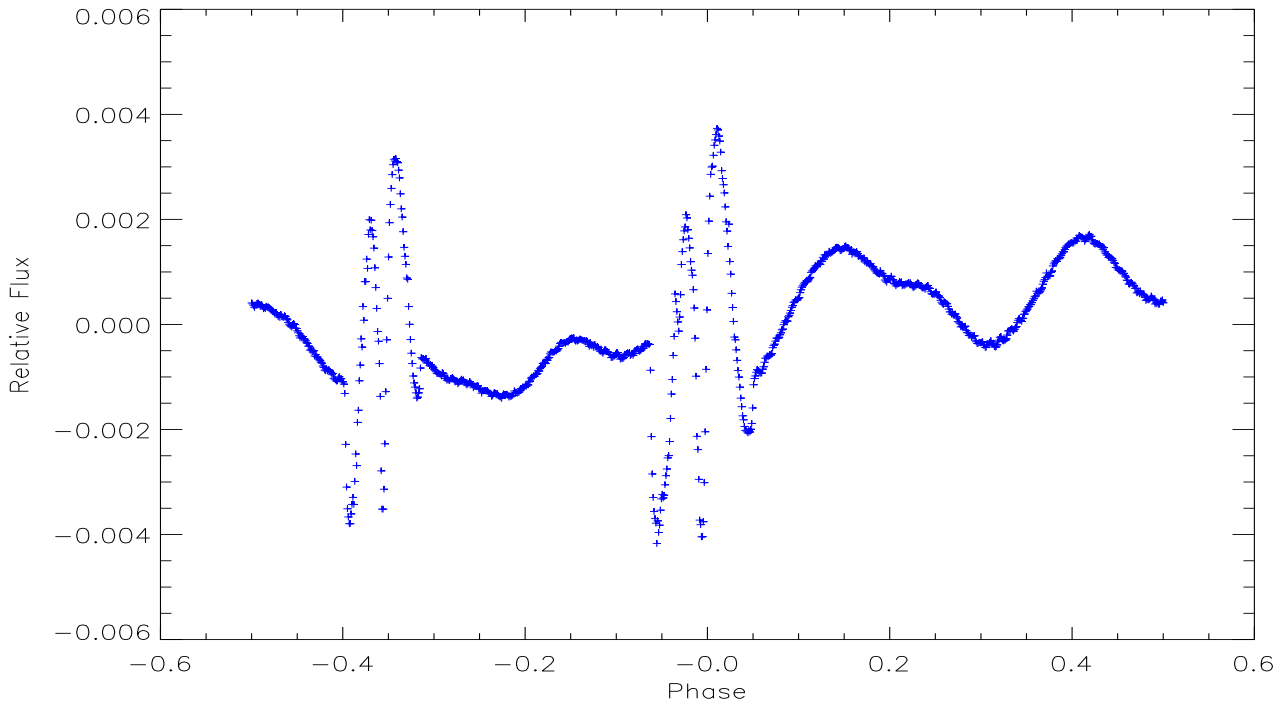


Figure 23: An image of the phase binned residuals of Quarter 7, following the first iteration with PHOEBE, with all the p modes removed and the g modes that are not orbital harmonics removed. The frequencies were prewhitened down to an amplitude of  $20 \mu\text{mag}$ , beyond which the frequencies could not be truly interpreted as real.

The frequency that is four times the orbital frequency is a prominent feature in the binned data and generates an obvious dip in the light curve between secondary and primary minimum. This feature recurs throughout the total data set ( $\nu_{orb} = 1.8279(1)$ ) and an explanation for its existence, other than that it is pulsation, is currently unavailable. *Thus we feel we have a clear case for a tidally excited mode for this frequency specifically and hence it is likely that other frequencies are also generated through the same mechanism.*

The frequencies identified that are the orbital frequency and two times the orbital frequency are not as easily attributed to tidal excitation. This is because, through masking the data there are gaps generated in the data will likely have a strong signal at these frequencies. It is also more likely that an imperfect fit to the data would generate peaks at such frequencies. Furthermore, peaks generated due to ellipsoidal variations occur on the time scale half the orbital period. Although it is likely that the model would fit any ellipsoidal variation that is present in the light curve this can not be thoroughly assumed.

Fig. 23 shows the Quarter 7 residuals with all the p modes removed and the g modes that are not orbital harmonics removed. This image further suggests, through the presence of what can only be

described as stellar oscillations in this residual data, that the harmonic frequencies are intrinsic to the star and are not generated by data processing. Furthermore, as the data have been phase binned by the orbital period, it can be clearly seen that these frequencies are strongly commensurate with the orbital period. The image displayed shows the residuals after the first iteration with PHOEBE; for this reason the eclipses have not been fitted completely as a consequence of all the pulsations being present in the light curve during the modelling process. However, this further highlights that the removal of frequencies and subsequent fitting did not inject this information into the light curve.

### 5.2.1 Frequency Separation Within the p Mode Regime

In KIC 4544587 the pattern of frequencies in the range between  $30 \text{ d}^{-1}$  and  $50 \text{ d}^{-1}$  is similar in appearance to those found in solar oscillators as there are multiple frequencies with equal separations as seen in the asymptotic p mode regime (See Fig. 24). Antoci et al. (in press) have recently identified p mode oscillations in a  $\delta$  Scuti star that are within the asymptotic regime. Hence, further investigations were required to determine whether the evident p mode pulsations in KIC 4544487 are also in the asymptotic regime where the frequencies can be quantified by the following expression:

$$\nu_{n,l} \approx \nu_0 \left( n + \frac{1}{2}l + \epsilon \right) + \delta\nu \quad (26)$$

where  $\nu$  is the p mode oscillation eigenfrequency,  $n$  and  $l$  are the overtone and degree of the mode,  $\epsilon$  is a small correction,  $\delta\nu$  is the small separation and  $\nu_0$  is the large separation, which is related to the speed of sound within the star and the radius of the star. Furthermore,  $\delta\nu$  is sensitive to the concentration of mass in the core and hence the age of the stellar component (Aerts et al., 2010).

In KIC 4544587 the average separation between the prominent frequencies in the p mode regime was found to be  $\sim 0.5 \text{ d}^{-1}$ . For a pulsations within the asymptotic regime to demonstrate such a small separation, where usual values are on the order of  $\sim 6 \text{ d}^{-1}$  for a main sequence A star (Heller & Kawaler, 1988), the rotation period of the star would have to be  $\sim 4$  hrs. This exceeds breakup velocity and thus rules out the possibility that these modes are within the asymptotic regime.

In Fig. 24 the dotted black lines are aligned with the dominant and second most dominant peaks respectively, and are separated by the orbital frequency ( $\nu = 0.456807 \text{ d}^{-1}$ ). In each figure it can clearly be seen that *many modes surrounding one of the two dominant peaks are separated from that peak by the orbital frequency*; although it can also be seen that all frequencies in the p mode regime do not have the same separation. A signature of the tidal locking hypothesis is a set of frequencies separated by the orbital frequency. However, symmetric multiplets are expected which are formed as a consequence of the stellar rotation, where as the frequencies observed do not demonstrate any obvious symmetry.

It is also worth noting that, unlike the case of KOI-54 where the resonant frequencies were 90 and 91 times the orbital frequency (Welsh et al., 2011), these frequencies are *not* orbital harmonics (with the exception of  $\nu = 44.3067(2)$  and  $\nu = 44.7595(5)$ ). Rather that  $(105.120635 \pm 0.000002) \times \nu_{orb}$  and  $(90.680309 \pm 0.000003) \times \nu_{orb}$  are the most and second most prominent p mode frequencies respectively. A list of values for all p mode frequencies can be seen in Table 12, which also includes both the frequency and size of the separation from the prominent modes in terms of the orbital frequency. The values that have a frequency separation from a dominant peak, equal to an integer multiple of the orbital frequency, are highlighted in blue (for a detection greater than two sigma) and red (for a detection greater than

Table 12: The p mode frequencies of Quarter 3.2 and the separation as a function of orbital period from the two most dominant p modes (highlighted in green). The values highlighted in blue demonstrate the p modes that are separated from one of the dominant modes by a multiple of the orbital frequency to an accuracy of over two sigma; and the red values show those separated to an accuracy of greater than three sigma. The frequencies divided by the orbital frequency are shown to demonstrate that the values being considered, with the exception of  $\nu = 44.3067(2)$  and  $\nu = 44.7595(5)$ , are not orbital harmonics. The values in parenthesis give the  $1\sigma$  uncertainty in the previous digit. The uncertainty in the amplitude is 0.0017 mmag

Frequency ( $\text{d}^{-1}$ )	Separation $/\nu_{orb}$	Frequency ( $\text{d}^{-1}$ )/ $\nu_{orb}$	Uncertainty ( $\text{d}^{-1}$ )/ $\nu_{orb}$	Amplitude (mmag)	Phase
In relation to the second most dominant p mode ( $\nu = 41.370 \text{d}^{-1}$ )					
38.2272(4)	6.8802(6)	83.68	0.000011	0.079	0.549(3)
39.5423(3)	4.0012(4)	86.56	0.000007	0.118	0.985(2)
39.9785(3)	3.0464(4)	87.52	0.000008	0.032	0.128(3)
40.0533(6)	2.8826(8)	87.68	0.000014	0.045	0.492(5)
41.3701(1)	-	90.56	0.000003	0.253	0.652(1)
41.4234 (3)	0.1166(5)	90.68	0.000008	0.033	0.136(3)
In relation to the most dominant p mode ( $\nu = 48.081 \text{d}^{-1}$ )					
42.9999(3)	10.9839(4)	94.13	0.000007	0.032	0.201(3)
43.26790(9)	10.3972(1)	94.72	0.000002	0.031	0.8796(8)
43.3928 (10)	10.1239(14)	94.99	0.000023	0.042	0.589(9)
43.4460(4)	10.0073(6)	95.11	0.000009	0.079	0.981(3)
43.4826(5)	9.9271(67)	95.19	0.000109	0.031	0.136(4)
44.3067(2)	8.1232(2)	96.99	0.000004	0.201	0.985(1)
44.3600(10)	8.0065(14)	97.11	0.000022	0.045	0.904(9)
44.7595(5)	7.1319(7)	97.98	0.000011	0.065	0.959(4)
44.8178(3)	7.0044(4)	98.11	0.000006	0.111	0.953(2)
44.8477(2)	6.9388(2)	98.18	0.000004	0.195	0.395(1)
44.9360(10)	6.7456(14)	98.37	0.000022	0.041	0.735(9)
46.1229(9)	4.1472(13)	100.97	0.000021	0.032	0.326(8)
46.1929(2)	3.9942(3)	101.12	0.000004	0.153	0.815(2)
46.5791(4)	3.1487(5)	101.97	0.000008	0.085	0.917(3)
46.6740(8)	2.9410(11)	102.17	0.000017	0.038	0.268(7)
46.75720(6)	2.7587(1)	102.36	0.000001	0.040	0.4760(5)
47.11179(7)	1.9825(1)	103.13	0.000002	0.038	0.9925(6)
47.5896(1)	0.9366(2)	104.18	0.0002	0.035	0.819(1)
47.9358(3)	0.1786(5)	104.94	0.000007	0.052	0.509(3)
47.9408(4)	0.1676(6)	104.95	0.000009	0.049	0.739(4)
47.9825(1)	0.0765(2)	105.04	0.000002	0.042	0.127(1)
48.0174(1)	-	105.12	0.000002	0.285	0.9868(9)
48.0590(7)	0.0911(10)	105.21	0.000014	0.050	0.611(6)

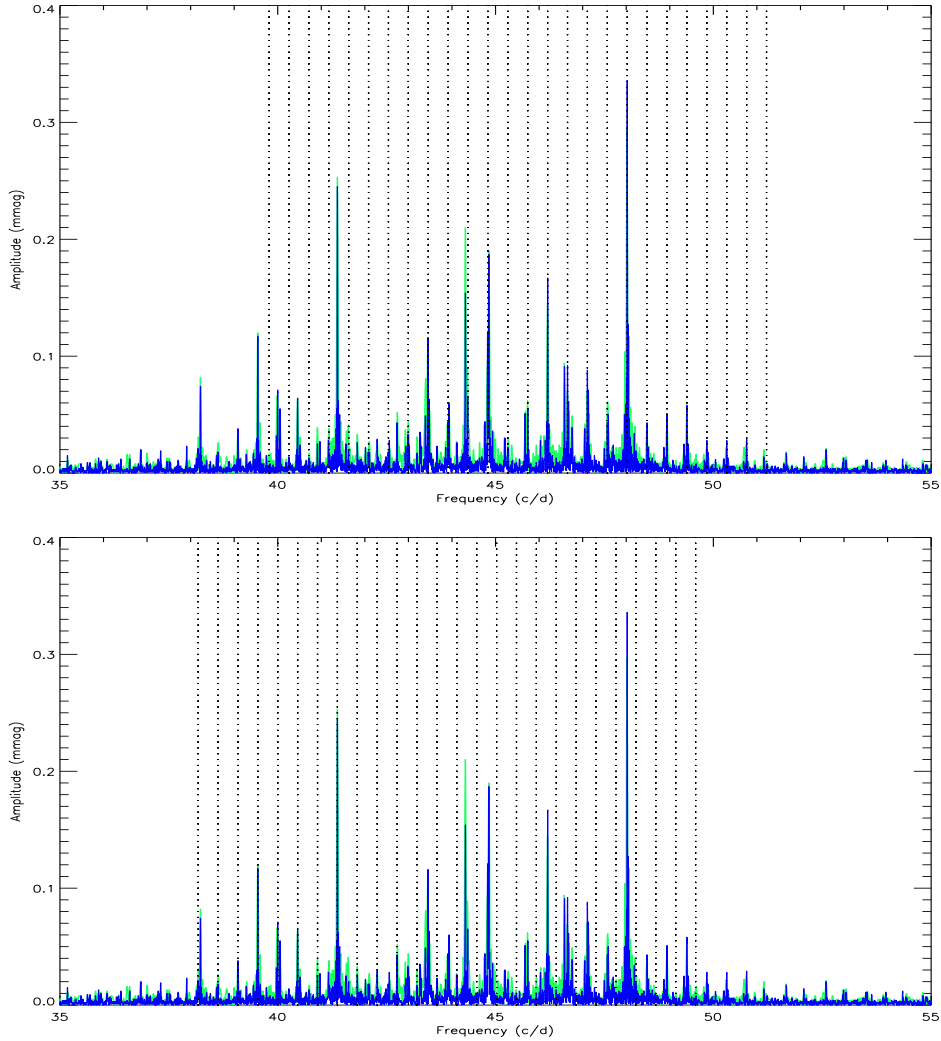


Figure 24: *Top panel:* A Fourier transform of the masked Quarter 3.2 residual data (green) and the masked Quarter 7 residual data (blue). The range of frequencies shown pertain to the p mode regime. The dashed black lines are aligned with the most prominent p mode ( $\nu = 48.0174(1) \text{ d}^{-1}$ ) and are equally separated by the orbital frequency ( $\nu = 0.4568070 \pm 0.0000005 \text{ d}^{-1}$ ). The Quarter 7 data has been converted into relative magnitudes to make a fair comparison. *Bottom panel:* A Fourier transform of the masked Quarter 3.2 residual data (green) and the masked Quarter 7 residual data (blue). The range of frequencies shown pertain to the p mode regime. The dashed black lines are aligned with the second most prominent p mode ( $\nu = 41.3701(1) \text{ d}^{-1}$ ) and are equally speared by the orbital frequency ( $\nu = 0.4568070 \pm 0.0000005 \text{ d}^{-1}$ ). Again, the Quarter 7 data has been converted into relative magnitudes to make a fair comparison.

three sigma). The two dominant peaks are highlighted in green. It is difficult to identify how this separation could be related to an inadequate orbital fit as opposed to the intrinsic nature of the star. This is further enhanced by the large number of three sigma detections surrounding the dominant peak. Currently we do not understand these peaks, but intend to work with theoreticians to produce an explanation in the future: this is a mystery!

### 5.3 Wavelet analysis

Wavelet analysis can be used to identify the stability of a frequency or frequencies, as a function of time, across a complete data set. We used a wavelet analysis program created by White et al. (2011) to

identify whether the modes found in KIC 4544587 were indeed stable. Special consideration was placed on frequencies that were harmonics of the orbital frequency and the p modes that are separated from a dominant mode by the orbital frequency.

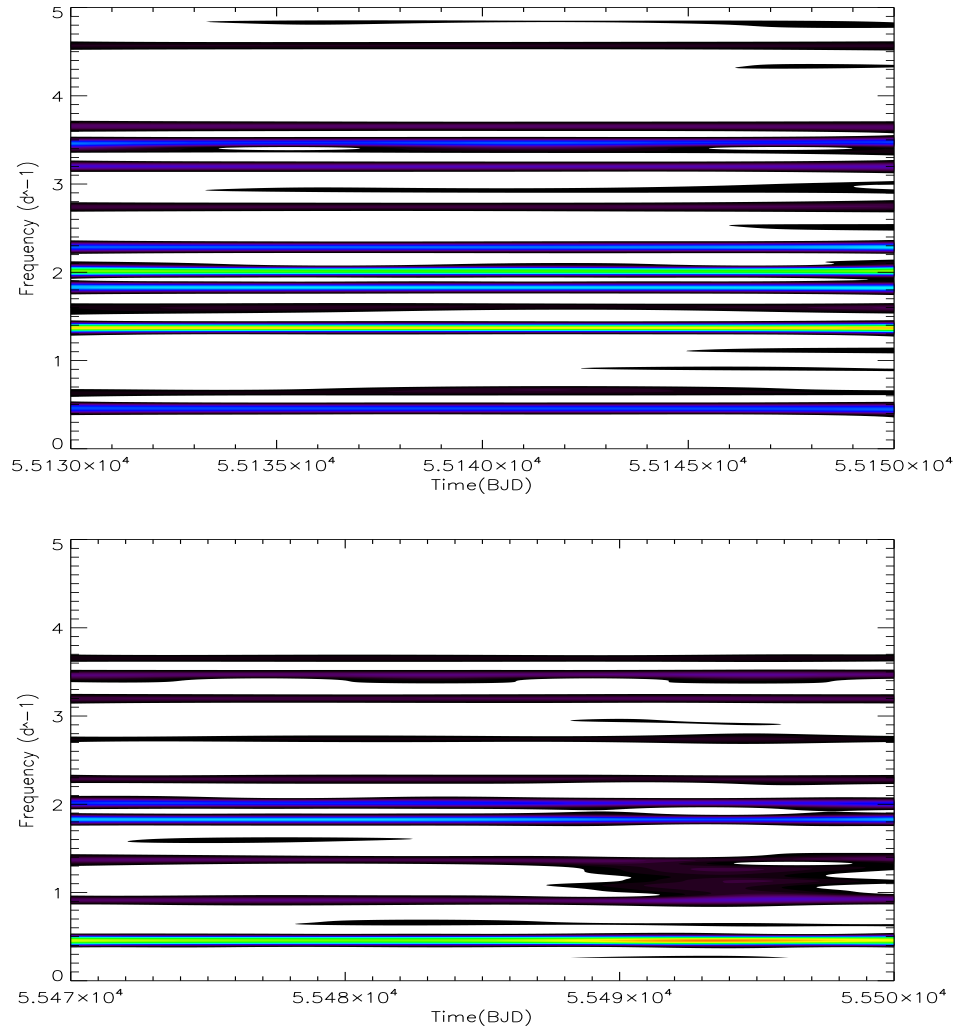


Figure 25: *Upper panel:* A wavelet analysis graph of data from Quarter 3.2 demonstrating the stability of the g mode pulsations. Here you can see that the majority of the frequencies are stable over a twenty day period. The scale on the time domain has been reduced from 30 d to 20 d due to the unreliable nature of the edges of wavelet analysis graphs. *Lower panel:* A wavelet analysis graph of data from Quarter 7 demonstrating the stability of the g mode pulsations. Here you can see that the majority of the frequencies are stable over a thirty day period. The scale on the time domain has been reduced to 30 d as the program is unable to read in the large number of data points pertaining to a whole quarter, and the edges were removed due to the unreliable nature of the edges of the wavelet analysis graphs. Orange is indicative of the highest amplitude peak and black of the lowest amplitude peak within the identified range of frequencies, and the time is in Barycentric Julian Date - 2 400 000.

We used the residuals from Quarter 3.2 and Quarter 7, which were generated using the Wilson-Devinney code and PHOEBE respectively. Initially the software reads in the data and requests input parameters including frequency range, step size and Gaussian width. A section of data is then selected and multiplied by a Gaussian of the specified width, to the data points within the time domain. A Fourier transform is applied to this section of the data for the specified frequency range and specified frequency resolution. The Gaussian is then shifted by the user specified time step and the process is repeated. This generates a set of files containing the identified frequencies and their corresponding

power for incrementing time values. The noise level for the data is also determined by performing a Fourier transform on the frequency range specified by the user as an are that is free of pulsation. This is used to determine the minimum power value in the data so that the colours can be scaled accordingly.

From these data files a graph is then generated, which displays time (in Truncated Barycentric Julian Date) on the x-axis and frequency ( $d^{-1}$ ) on the y-axis. The various colours represent power and hence the power of a frequency as a function of time can be identified (where black is the lowest and orange is the highest amplitude peak).

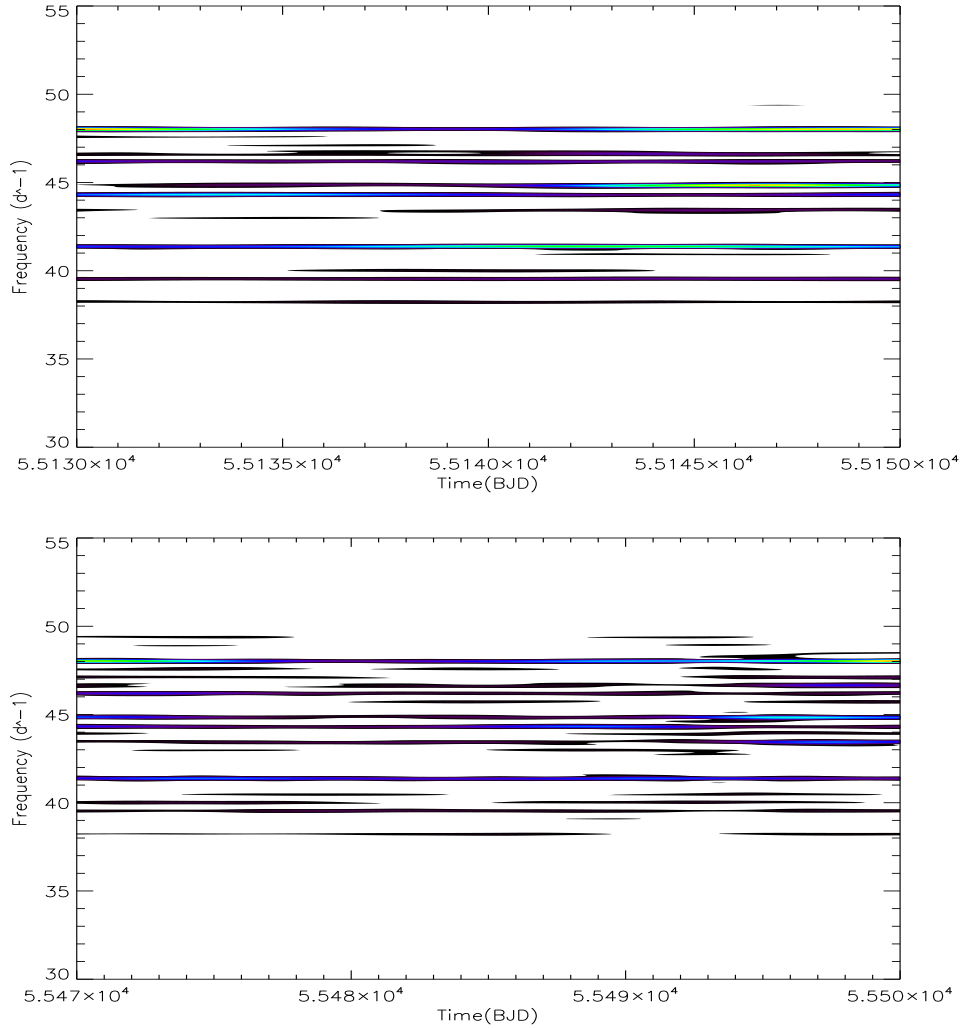


Figure 26: *Upper panel:* A wavelet analysis graph of data from quarter 3.2 demonstrating the stability of the prominent p mode pulsations. Here you can see that the majority of the frequencies are stable over a twenty day period. The scale on the time domain has been reduced from 30 d to 20 d due to the unreliable nature of the edges of the wavelet analysis graphs. *Lower panel:* A wavelet analysis graph of data from Quarter 7 demonstrating the stability of the g mode pulsations. Here you can see that the majority of the frequencies are stable over a thirty day period. The scale on the time domain has been reduced to 30 d as the program is unable to read in the large number of data points pertaining to a whole quarter, and again the edges were removed due to the unreliable nature of the edges of the wavelet analysis graphs. The time is in Barycentric Julian Date - 2400 000 and orange is indicative of the highest amplitude peak and black of the lowest amplitude peak within the identified range of frequencies.

When determining the input values for the wavelet analysis there were some details that required consideration. These include the width of the Gaussian with respect to the size of the total data set and

the number of cycles encompassed within each Gaussian, for the modes within the range of frequencies being considered, in the time domain. If the Gaussian was large with respect to the size of the data set it would not show a large amount of variation as a function of time. If the Gaussian was too small then the Fourier transform would suffer bad aliasing effects. It was found that a Gaussian width of 10 hr was under-sampling the data to an extreme extent, which created a blob effect as opposed to a continuous pattern. Furthermore, the edge effects became more prominent, again due to under-sampling caused by the width of the Gaussian. It is worth noting that the edges of wavelet analysis graphs have been removed as they do not contain reliable data.

The time step between successive Gaussians also had to be considered, as if this were too large then the resolution of the graph in the time domain would be poor, conversely, a small time step is highly expensive in computational time. The number of frequencies selected pertains to the number of successive steps in the y-direction. For the wavelet graphs presented a frequency resolution of 1000 was used, this corresponds to a resolution of 200 frequencies per increment of one cycle per day for the g mode graphs (frequency range between 0–5 d<sup>-1</sup>) and 40 frequencies per increment of one cycle per day for the p mode graphs, which cover a larger frequency range (frequency range between 30–50 d<sup>-1</sup>).

Fig. 25 demonstrate the amplitude of the g mode frequencies as a function of time. It can be seen that the prominent peaks in the two quarters are different: in Quarter 3.2 the prominent mode is 1.37 d<sup>-1</sup>;  $3\nu_{orb}$  and in Quarter 7 the prominent mode is the orbital frequency. It is possible that both frequencies, or at least the prominence them, could be attributed to an inadequate fit. However, the dominance of the orbital frequency in Quarter 7 is more likely present due to the orbital characteristics than the dominance of a frequency that is  $3\nu_{orb}$  in Quarter 3.2. Primarily because the results of Quarter 7 are only preliminary at this stage.

In Quarter 3.2 there appear to be multiple peaks at higher frequency range of the g mode region. Most of the dominant modes present in both quarters appear stable over the duration of the quarter. However, there appear to be several low amplitude peaks that are not stable. This could be due to events intrinsic to the star such as mass loss. The subsequent thorough analysis of the Quarter 7 residuals will enable a direct comparison of the two quarters and hence allow the determination of the stability of these modes across the different quarters.

In Fig. 26 there are six prominent modes that are constant for the duration of each of the data sets and consistent over the two data sets. The modes identified coincide with the 6 highest amplitude peaks identified in the p mode range of the Fourier transform of the Quarter 3.2 residuals, which are: 48.0174(1) d<sup>-1</sup>, 41.3701(1) d<sup>-1</sup>, 44.3067(2) d<sup>-1</sup>, 44.8477(2) d<sup>-1</sup>, 46.1929(2) d<sup>-1</sup>, 39.5423(3) d<sup>-1</sup> (where the value in the parentheses gives the one sigma uncertainty in the previous digit). Five of the six peaks are those identified as forming the set of frequencies that are separated from the dominant p modes by the orbital frequency. Moreover, while two are the dominant modes, from which the separation is measured, a further two are separated by a multiple of the orbital frequency to an accuracy greater than  $3\sigma$  with the third being well within the  $2\sigma$  threshold.

## 6 Conclusions

The analysis of KIC 4544587 has been undertaken to determine the binary characteristics of the system and identify the pulsation frequencies inherent in the components. Quarter 3.2 SC data have been modelled thoroughly using the WD code and frequency analysis has been performed on the residual data. The Quarter 7 SC data have been modelled, using PHOEBE, to the extent that information can be inferred about the binary characteristics and preliminary results have been obtained in the frequency analysis. Future work will include the completion of the analysis of Quarter 7 and Quarter 8 with the incorporation of spectroscopically defined values (effective temperature,  $\log g$  and metallicities) and a radial velocity curve in the the modelling process.

Initially the period of the binary system was found using the PDM technique (Stellingwerf, 1978). This technique determines the period of the system by phase binning the data by a possible period and comparing the variance of the binned data to the variance of the total data set. Using PDM the period of Quarter 3.2 was found to be  $P = 2.1891142(5)$  d, Quarter 7 was found to be  $P = 2.1891122(5)$  d and the period of the total data set was found to be  $P = 2.1891101(5)$  d. The periods concur to 6 significant figures, although the slight deviation in the values was an initial indication that the system was undergoing apsidal advance at a rate that was significant with respect to the duration of the data set.

JKTEBOP was then applied to the Quarter 3.2 data to obtain initial parameter estimates for the subsequent binary modelling and to further constrain the orbital ephemeris. Upon acquisition of the Quarter 7 data, the ephemeris of Quarter 7 was also determined. The results generated for the ephemerides were consistent with those generated using the PDM technique to  $4\sigma$ . However, the zero points of the two ephemerides did not concur with each other. This further suggested that the system is undergoing apsidal advance at a rate that is noticeable over the time scale of the data obtained.

The orbital characteristics of the Quarter 3.2 data were then modelled using the WD code. Initially no constraints were placed on the modelling so that a fit to the data with a minimal amount of residuals could be achieved. Primarily this allowed an orbital fit to be generated without consideration of the coupling of the temperatures and luminosities of the components. Once an initial orbital fit had been generated, the model was subtracted from the data and frequency analysis was performed on the residual data. The identified frequencies were then prewhitened from the data allowing for a second iteration where the orbital characteristics were modelled without interference from the pulsations. Finally, a third iteration was undertaken which determined the orbital characteristics of KIC 4544587 and generated a set of residuals upon which thorough frequency analysis was performed. On the third iteration the temperatures and luminosities of the two components were coupled so that the temperatures and luminosities, and thus model generated obeyed the Stefan-Boltzmann law.

For the Quarter 7 data the aforementioned process was repeated. However, PHOEBE was incorporated into the modelling process and the temperatures and luminosities were coupled throughout the fitting process. Although the analysis of Quarter 7 is not yet complete, information can still be inferred about the different approaches from the binary modelling perspective as the final iteration has the largest impact on the frequency analysis.

One of the most significant differences found between the two data sets was that the orbital results of Quarter 3.2 are suggestive of a binary companion that is an early G star with a convective outer envelope

and the orbital results of Quarter 7 are indicative of a late F star with a radiative outer envelope. It is possible that this is a direct consequence of the different methods, specifically the coupling of the temperatures and luminosities in the initial modelling stages. It is also possible, however, that a local minimum was identified in one of the modelling approaches as opposed to the global minimum. The acquisition of the temperatures through spectroscopy will enable the identification of the floors in both approaches and further highlight the best approach. Consequently this will lead to an improved understanding of the best approach to modelling binary systems that contain pulsation, which alter the shape of the light curve.

The possibility of rotation other than pseudo-synchronous rotation was then investigated by altering PHOEBE's synchronicity parameter when modelling the Quarter 7 data. Using the formula defined by Hut (1981), the quasi-synchronous rotation value for KIC 4544587 was obtained ( $F = 1.87(1)$ ). The synchronicity parameter was held fixed and also fitted during the modelling process in an attempt to constrain an improved orbital model. The quality of the fit to the data decreased on each occasion, with the formation of a trough in the residuals between secondary and primary eclipse. Consequently the synchronicity parameter was fixed at 1.0 for the remainder of the fitting process which is indicative of a pseudo-synchronous system.

The apsidal advance of the system was then investigated. This was done initially by determining the anomalous period of the complete data set, which was found to be  $\sim 2.189096$  d. The existence of an anomalous period, where the secondary eclipse appears smeared whilst the primary eclipse is precisely defined in phase space, demonstrated that the system is undergoing apsidal advance. Following this the rate of apsidal advance was determined by modelling the data using PHOEBE. The rate of apsidal advance was found to be  $0.0001179(1)$  rad d $^{-1}$ , which gives  $145.9(1)$  yr for one complete precession. Future work will include the determination of the constant,  $k_2$ , from which the ratio of the mean to central density can be determined.

Frequency analysis was performed on Quarter 3.2 residuals and compared with preliminary results from Quarter 7. Dominant modes were identified in the p mode regime and the g modes regime for both quarters. The residuals were masked, by removing data points during the eclipse phases so that any remnant orbital information was not incorporated into the frequency analysis. In the Quarter 3.2 data 15 frequencies were identified as harmonics of the orbital frequency, 9 of which are in the g mode regime and 6 in the p modes regime. *This is a signature of tidal resonance.*

For a  $\delta$  Scuti star, a pulsation constant of  $Q = 0.033$  is indicative of the fundamental radial mode. Using the relation between period and density, the fundamental frequency of the A-type star in KIC 4544587, which we assume is the pulsating star (although future spectroscopic data will confirm this), has a frequency of  $13.9 \pm 2.5$  d $^{-1}$ . There are no frequencies in the residuals of Quarter 3.2 or Quarter 7 in this region suggesting that the  $\delta$  Scuti component of KIC 4544587 does not pulsate in the fundamental radial mode. Future collaboration with asteroseismic modelling teams will unveil the physical nature of the frequencies identified in KIC 4544587.

In the p mode regime it was determined that many of the frequencies were separated from the the two dominant p modes by multiples of the orbital frequency. Many of the frequencies (five with respect to the dominant p mode) demonstrate this separation to an accuracy of  $3\sigma$  or greater. Furthermore, these frequencies are not orbital harmonics. The origin of these frequencies is yet unknown: they are a mystery! However, the wavelet analysis of these frequencies suggests that they are stable over Quarter 3.2 and

Quarter 7. Future analysis will include working with theoreticians to develop a theory for the existence of such pulsations, currently we know of no other star that demonstrates these characteristics.

Through the analysis of KIC 4544587 we have identified frequencies that are signatures of tidal resonance. On a preliminary basis, we have confirmed the existence of radiative damping with dynamic tides through the identification of resonant pulsations. Subsequent spectroscopic data will confirm these results leading to one of only a handful of observations demonstrating tidal resonance. Upon acquisition of spectroscopic data, future work will involve incorporation of the spectra into our current models following which the findings will be published.

## 7 Acknowledgements

I would like to thank Prof. Don Kurtz for his supervision and support throughout this project. I would also like to thank my collaborators, Andrej Prša, Steven Bloemen and John Southworth for their time and effort which enabled the successful completion of this work.

I would like to thank the *Kepler* team for allowing me to work with and analyse the *Kepler* data, without whom this project would not have been possible. Funding for the *Kepler* mission is provided by NASA's Science Mission Directorate, for which I am thoroughly grateful. I would also like to thank the Jeremiah Horrocks Institute and the Royal Astronomical Society for their generosity in funding my attendance at conferences.

## References

- Abt, H. A. 2009, *AJ*, 138, 28
- Abt, H. A., & Hudson, K. I. 1971, *ApJ*, 163, 333
- Aerts, C., Christensen-Dalsgaard, J., & Kurtz, D. 2010, *Astroseismology* (Springer)
- Aerts, C., & Harmanec, P. 2004, in *Astronomical Society of the Pacific Conference Series*, Vol. 318, *Spectroscopically and Spatially Resolving the Components of the Close Binary Stars*, ed. R. W. Hilditch, H. Hensberge, & K. Pavlovski, 325
- Amado, P. J., Moya, A., Suárez, J. C., Martín-Ruiz, S., Garrido, R., Rodríguez, E., Catala, C., & Goupil, M. J. 2004, *MNRAS*, 352, L11
- Andersen, J. 1991, *A&AR*, 3, 91
- Antoci, V., et al. 2011, *ArXiv e-prints*, 1109.4285
- Baglin, A., et al. 2006, in *COSPAR, Plenary Meeting*, Vol. 36, 36th COSPAR Scientific Assembly, 3749
- Borucki, W. J., Koch, D., Basri, G., Batalha, N., Brown, T., Caldwell, D., & et al. 2010, *Science*, 327, 977
- Breger, M. 1970, in *Bulletin of the American Astronomical Society*, Vol. 2, *Bulletin of the American Astronomical Society*, 298
- Breger, M. 1990, *Delta Scuti Star Newsletter*, 2, 13
- Breger, M. 2000, in *Astronomical Society of the Pacific Conference Series*, Vol. 210, *Delta Scuti and Related Stars*, ed. M. Breger & M. Montgomery, 3
- Buzasi, D. L., et al. 2005, *ApJ*, 619, 1072
- Caldwell, D. A., Kolodziejczak, J. J., Van Cleve, J. E., Jenkins, J. M., Gazis, P. R., Argabright, V. S., & et al. 2010, *ApJ*, 713, L92
- Claret, A. 2001, *MNRAS*, 327, 989
- Cowling, T. G. 1938, *MNRAS*, 98, 734
- Cowling, T. G. 1941, *MNRAS*, 101, 367
- Crowther, P. A., Schnurr, O., Hirschi, R., Yusof, N., Parker, R. J., Goodwin, S. P., & Kassim, H. A. 2010, *MNRAS*, 408, 731
- Cunha, M. S., et al. 2007, *A&AR*, 14, 217
- Darwin, G. H. 1880, *Astronomische Nachrichten*, 96, 217
- Diaz-Cordoves, J., & Gimenez, A. 1992, *A&A*, 259, 227
- Eddington, A. S. 1926, *MNRAS*, 86, 320
- Eddington, A. S. 1930, *The Observatory*, 53, 208

- Etzel, P. B. 1981, in *Photometric and Spectroscopic Binary Systems*, ed. E. B. Carling & Z. Kopal, 111
- Fabian, A. C., Pringle, J. E., & Rees, M. J. 1975, *MNRAS*, 172, 15P
- Fath, E. A. 1940, *Lick Observatory Bulletin*, 19, 77
- Gilliland, R. L., Brown, T. M., Christensen-Dalsgaard, J., Kjeldsen, H., Aerts, C., & et al. 2010, *PASP*, 122, 131
- Grigahcène, A., et al. 2010a, *Astronomische Nachrichten*, 331, 989
- Grigahcène, A., Uytterhoeven, K., Antoci, V., Balona, L., Catanzaro, G., & et al. 2010b, *Astronomische Nachrichten*, 331, 989
- Guzik, J. A., Kaye, A. B., Bradley, P. A., Cox, A. N., & Neuforge, C. 2000, *ApJ*, 542, L57
- Heller, C. H., & Kawaler, S. D. 1988, *ApJ*, 329, L43
- Houdek, G. 2000, in *Astronomical Society of the Pacific Conference Series*, Vol. 210, *Delta Scuti and Related Stars*, ed. M. Breger & M. Montgomery, 454
- Hut, P. 1980, *A&A*, 92, 167
- Hut, P. 1981, *A&A*, 99, 126
- Jenkins, J. M., et al. 2010, *ApJ*, 713, L87
- Kallrath, J. 2009, *Eclipsing Binary Stars: Modeling and Analysis* (2 ed.) (Springer)
- Kjeldsen, H., & Bedding, T. R. 2011, *A&A*, 529, L8
- Kjeldsen, H., Christensen-Dalsgaard, J., Handberg, R., Brown, T. M., Gilliland, R. L., Borucki, W. J., & Koch, D. 2010, *Astronomische Nachrichten*, 331, 966
- Klinglesmith, D. A., & Sobieski, S. 1970, *AJ*, 75, 175
- Kumar, P., Ao, C. O., & Quataert, E. J. 1995, *ApJ*, 449, 294
- Kurtz, D. W. 1980, *MNRAS*, 193, 61
- Kurtz, D. W. 1982, *MNRAS*, 200, 807
- Kurtz, D. W. 1985, *MNRAS*, 213, 773
- Latham, D. W., Brown, T. M., Monet, D. G., Everett, M., Esquerdo, G. A., & Hergenrother, C. W. 2005, in *Bulletin of the American Astronomical Society*, Vol. 37, *American Astronomical Society Meeting Abstracts*, 110.13
- Lee, Y.-H., Kim, S. S., Shin, J., Lee, J., & Jin, H. 2008, *PASJ*, 60, 551
- Lefèvre, L., et al. 2009, *Communications in Asteroseismology*, 158, 189
- Lenz, P., & Breger, M. 2004, in *IAU Symposium*, Vol. 224, *The A-Star Puzzle*, ed. J. Zverko, J. Ziznovsky, S. J. Adelman, & W. W. Weiss, 786

Lucy, L. B. 1967, ZEASAJ, 65, 89

Maceroni, C., et al. 2009, A&A, 508, 1375

Mathias, P., Gillet, D., Aerts, C., & Breitfellner, M. G. 1997, A&A, 327, 1077

Milne, E. A. 1926, MNRAS, 87, 43

Moreno, E., Koenigsberger, G., & Harrington, D. M. 2011, A&A, 528, A48

Nelson, B., & Davis, W. D. 1972, ApJ, 174, 617

Pamyatnykh, A. A. 1999, A&A, 49, 119

Pamyatnykh, A. A. 2000, in *Astronomical Society of the Pacific Conference Series*, Vol. 210, *Delta Scuti and Related Stars*, ed. M. Breger & M. Montgomery, 215

Petersen, J. O., & Christensen-Dalsgaard, J. 1996, A&A, 312, 463

Pigulski, A. 2006, in *Astronomical Society of the Pacific Conference Series*, Vol. 349, *Astrophysics of Variable Stars*, ed. C. Aerts & C. Sterken, 137

Popper, D. M. 1984, AJ, 89, 132

Popper, D. M., & Etzel, P. B. 1981, AJ, 86, 102

Press, W. H., & Teukolsky, S. A. 1977, ApJ, 213, 183

Prša, A. 2005, Ph.D. thesis, University of Ljubljana

Prša, A., & Zwitter, T. 2005, ApJ, 628, 426

Quataert, E., Kumar, P., & Ao, C. O. 1995, in *Bulletin of the American Astronomical Society*, Vol. 27, *American Astronomical Society Meeting Abstracts*, 1343

Reed, M. D., & Brondel, B. J. 2005, in *Astronomical Society of the Pacific Conference Series*, Vol. 333, *Tidal Evolution and Oscillations in Binary Stars*, ed. A. Claret, A. Giménez, & J.-P. Zahn, 228

Rodríguez, E., & Breger, M. 2001, A&A, 366, 178

Ruciński, S. M. 1969, *Acta Astron.*, 19, 245

Russell, H. N., & Merrill, J. E. 1952, *The determination of the elements of eclipsing binaries*

Schwarzenberg-Czerny, A. 1989, MNRAS, 241, 153

Southworth, J. 2008, MNRAS, 386, 1644

Southworth, J., Maxted, P. F. L., & Smalley, B. 2004a, MNRAS, 349, 547

Southworth, J., Maxted, P. F. L., & Smalley, B. 2004b, MNRAS, 351, 1277

Southworth, J., Smalley, B., Maxted, P. F. L., Claret, A., & Etzel, P. B. 2005, MNRAS, 363, 529

Southworth, J., et al. 2011, MNRAS, 414, 2413

- Stellingwerf, R. F. 1978, *ApJ*, 224, 953
- Stellingwerf, R. F. 2010, *PDM2*
- Sterne, T. E. 1939, *MNRAS*, 99, 662
- Torres, G., Andersen, J., & Giménez, A. 2010, *A&AR*, 18, 67
- Van Cleve, J. E. 2009 (Moffet Field CA: NASA Ames Research Center)
- Vogt, H. 1926, *Astronomische Nachrichten*, 226, 301
- von Zeipel, H. 1924, *MNRAS*, 84, 702
- Walker, G., et al. 2003, *PASP*, 115, 1023
- Welsh, W. F., et al. 2011, *ArXiv e-prints*, 1102.1730
- White, T. R., Bedding, T. R., Stello, D., Kurtz, D. W., Cunha, M. S., & Gough, D. O. 2011, *MNRAS*, 415, 1638
- Willems, B., & Aerts, C. 2002, in *Astronomical Society of the Pacific Conference Series*, Vol. 259, IAU Colloq. 185: Radial and Nonradial Pulsations as Probes of Stellar Physics, ed. C. Aerts, T. R. Bedding, & J. Christensen-Dalsgaard, 76
- Wilson, R. E. 1979, *ApJ*, 234, 1054
- Wilson, R. E., & Devinney, E. J. 1971, *ApJ*, 166, 605
- Wilson, R. E., & Sofia, S. 1976, *ApJ*, 203, 182
- Wilson, R. E., & Van Hamme, W. 2004, *Computing Binary Star Observables (Wilson-Devinney program user guid)*
- Zahn, J.-P. 1975, *A&A*, 41, 329
- Zahn, J.-P. 1977, *A&A*, 57, 383

## A Appendix

The following information has been included for reference purposes for myself or anyone wishing to use the software discussed.

### Fourier Transform: FTday

The program psd2010.for generates frequency, amplitude and phase information pertaining to the highest peak in the Fourier transform (hereafter FT) each time it is run. Furthermore, it generates a file containing the observed minus calculated data (the input data minus the frequencies calculated) and a file containing the Fourier transform data. Previously known frequencies can be placed in the input file which are prewhitened from the data prior to further analysis. This allows for an iterative process whereby each time the maximum peak is located, it can be placed in the input file and thus will be prewhitened from the data prior to the identification of the next largest peak. The input file is called FTday.com and contains the following:

- The first line contains the the directory of the psd2010.for file that needs to be amended accordingly.
- The second line contains the name of the data file.
- The third line contains the zero point of the data (from which the phase is measured).
- The fourth line contains the number of frequencies contained in the file.
- All other lines(except the final two) contain the aforementioned frequencies that are pre-established, with their amplitudes (in the same units as the input file) and phase.
- The second to final line contains the frequency range followed by the step value. The frequency range is specified as a function of step value (i.e. 300 500 0.01 is 3 to 5 in steps of 0.01) where the units are defined as 1/the time units of the input data.
- Then final line has a star to denote the end of the file

The output for this file can be printed to the screen or piped to a new file. It contains:

- T0: The zero point value entered in the executable file
- Faver: the average value of all the data points
- npts: the number of points
- difft(hrs): the total time in hrs
- sigma: The overall variation
- Frequency, amplitude and phase values, for the range of values specified in the executable file.
- The frequency, amplitude and phase of the maximum peak (separate from other lines)
- Frequency, amplitude and phase for all time step, as specified in the input file.

Furthermore, the two files containing the Fourier transform data and the observed minus computed data, are fort.16 and fort.19 respectively.